

Gravitational Waves from Collapse of Pressureless Matter in the Early Universe

Ioannis Dalianis^a and Chris Kouvaris^b

^a *Department of Physics, University of Cyprus,
Nicosia 1678, Cyprus*

^b *Physics Division, National Technical University of Athens
15780 Zografou Campus, Athens, Greece*

Abstract

If an early matter phase of the Universe existed after inflation with the proper power spectrum, enhanced density perturbations can decouple from the Hubble flow, turn around and collapse. In contrast to what happens in a radiation dominated Universe where pressure nullifies deviations from sphericity in these perturbations, in a matter dominated Universe, the lack of pressure although on the one hand facilitates the gravitational collapse, it allows small deviations from sphericity to grow substantially as the collapse takes place. The subsequent collapse is complicated: initially as non-spherical deviations grow, the collapsing cloud takes the form of a “Zel’dovich pancake”. After that, the more chaotic and nonlinear stage of violent relaxation begins where shells of the cloud cross and the matter is redistributed within a factor of a few of the free fall timescale, reaching a spherical virialized state. During the whole process, strong gravitational waves are emitted due to the anisotropy of the collapse and the small time interval that the effect takes place. The emission of gravitational waves during the stage of the violent relaxation cannot be easily estimated with an analytical model. We perform an N -body simulation to capture the behaviour of matter during this stage in order to estimate the precise spectrum of gravitational waves produced in this scenario.

1 Introduction

Strong gravitational waves (GWs) can be emitted during a gravitational collapse if the collapse involves aspherical and rapid motion of dense matter distributions [1]. Astrophysical systems are common examples of strong gravitational sources. Presumably, such conditions are also found in the dense and energetic early Universe if there are sufficiently large density perturbations. Primordial density perturbations are observed at CMB scales through temperature anisotropies and have a minute size. At small scales the amplitude of density perturbations is not measured and it might be significantly larger [2–7]. Deviations from homogeneity in the primordial Universe can result in gravitational instabilities and perturbative GW emission [8,9]. Furthermore, if an early matter domination era (EMD) has been realized, the density perturbations grow further and in the absence of background pressure an isotropic evolution cannot be supported. As a result, an additional strong GW component is generated during the process of matter compression and virialization, leading possibly to the formation of ephemeral halos. GW emission of this sort, that involves pressureless bulk mass motion, is not expected for smooth unclustered energy components, like radiation, that is understood to collapse and expand isotropically.

During an EMD era the pressure is vanishing and deviations from sphericity are assumed for the primordial density perturbations that enter the horizon. Initially in the linear regime,

the perturbations evolve in the expanding background and asphericity grows. At some point the expansion of the overdensities is expected to halt along the dimension that the compression is maximal and collapse follows. The first stage of gravitational evolution can be described by the “pancake formation” process, developed by Zel’dovich [10]. The Zel’dovich approximation is a theory for the growth and evolution of density cosmological perturbations in the nonlinear stage and in a background of zero pressure. Central quantities are a deformation tensor D_{ij} , that describes the non-spherical geometrical profiles of density perturbations, and a probability density function (PDF) associated with the statistical significance of the aspherical configurations. Assuming an initial Gaussian distribution for the perturbations, probabilities of the various initial profiles can best be obtained using the Doroshkevich PDF [11].

We will consider and study the evolution of a gravitational instability originated from strong linear perturbations in an expanding EMD Universe. Our main focus is on the gravitational radiation emitted during the anisotropic motion of matter which deviates from the background Hubble flow. The spectrum of the GWs produced in the first stages, during which the inhomogeneity decouples from the background expansion and experiences a pressureless collapse, has been computed in ref. [12]. In that first paper, the analytical expression for the spectrum of stochastic GW background has been given in the post-Newtonian framework which describes the GW emission during the entire course of the evolution of the inhomogeneity. The computation of the spectrum was done assuming the Zel’dovich solution that is valid roughly until the limiting stage of the pancake collapse. This limitation on the description of the nonlinear evolution calls for more sophisticated numerical approaches and motivates the current work. In this paper we take a step forward and complement our previous results [12] by tracking the evolution of the inhomogeneities deep in the nonlinear regime via numerical means. We utilize N -body techniques which provide a unique theoretical tool that opens up the way to go beyond the analytic approximations. The underlying assumption made is that the fluid which realizes the EMD era can be simulated by a distribution of individual nonrelativistic particles. Via N -body simulations we find that the dynamical evolution of the perturbation into nonlinear structures involves bulk mass motions that source GW emission, occasionally with pretty large amplitude. We compute the quadrupole for the mass distribution and obtain the spectrum of GWs from the moment of horizon entry of the perturbation until the stage of nonlinear clustering.

We use the publicly available Nbody2 code of Aarseth [13], which is a Newtonian gravity N -body code, to run our simulations. The spectrum pattern of GWs emitted by subhorizon modes is found to depend significantly on the initial conditions that characterize the geometry of the density perturbations. The spatial structure of the initial density and velocity perturbations are specified by the deviation of the density perturbations σ and the parameters (α, β, γ) of the deformation tensor D_{ij} . These parameters define a particular configuration and determine our initial conditions for the N -body simulations. We assume small-scale perturbations with wavelength $k^{-1} \ll 1 \text{ Mpc}^{-1}$ and a large deviation $0.005 \lesssim \sigma \lesssim 0.2$, so as the processes involved to have potentially observable implications. We track and describe the cosmological collapsing processes running the N -body system for sufficiently many crossing times. We observe that the collapsing matter undergoes violent relaxation and settles into an equilibrium configuration. After the completion of the phase mixing and relaxation process we observe that a halo forms which satisfies the virial theorem, i.e. virialization takes place.

The gravitational emissivity is found to be very sensitive to the geometrical features, determined by the deformation parameters (α, β, γ) and σ of the density perturbation. A Hubble patch that encloses a perturbation with an acute nonspherical profile emit GWs with a power several orders of magnitude larger than a patch with an approximate spherical profile. The probability for each profile to be realized also varies significantly and is determined by the Doroshkevich PDF, so that profiles with extreme parameters are extremely rare. The average GW spectrum is found after a summation procedure, that takes into account the statistical significance of each configuration. The observable average spectrum is cosmology dependent. Aside from the σ value, it is specified after values for the mass of the perturbation M and the

reheating temperature T_{rh} are given. In particular, the overall frequency is specified by the mass M parameter, which is associated with the wavenumber position k of the curvature spectrum peak $\mathcal{P}_{\mathcal{R}}(k)$. Here we will consider curvature power spectra peaks that are dominantly monochromatic with amplitude $\sim \sigma^2$. Both amplitude and frequency have also an overall dependence on the duration of the EMD phase parameterized by the T_{rh} value.

We run the N -body simulation with initial positions and velocities for the particle distribution specified at the moment of maximum expansion of the inhomogeneity t_{max} which is the moment in time that the first turnaround occurs, set to be along the axis r_1 . We adopt the Zel'dovich solution, which we consider reliable enough until the time of the turnaround. Zel'dovich solution for determining initial positions and velocities have been also used elsewhere [14]. However, we observe that the accuracy of the Zel'dovich description is gradually lost until the stage of the pancake collapse t_{col} and eventually breaks down. As expected the spectrum of the produced GWs found from the N -body results has similarities to the spectrum found using the Zel'dovich solution [12] only for times before the pancake collapse and it is characterized by a rough single peak associated with the undergoing quadrupole changes.

Going beyond the stage of pancake collapse, the N -body simulation reveals a new dynamical evolution. The distribution of N -particles experiences a violent relaxation that drives it, sooner or later, towards a quasi-steady spherical configuration. This stage produces GWs that might or might not surpass the amplitude produced during the first stage of pancake collapse. In particular, initial configurations with a mostly spherical shape reach the virialized state in a time t_{vir} roughly twice the time of pancake collapse without increasing the amplitude of the final GW spectrum much. Configurations with acute asymmetry experience a second collapse after the pancake stage. Fast rearrangements of the mass distribution result in an enhanced amplitude for the GW spectrum and produce additional spectral peaks. The maximal enhancement is found to reach one order of magnitude in size. The notable features are clearly observed in configurations that experience an oblate-prolate geometrical change during the course of virialization. These geometrical changes generate a second rough peak in the GW spectrum at a larger frequency with a value associated with the duration of the violent relaxation process. This second peak gets modulated or even disappears as we change the values for the deformation parameters α, β and γ . The emission of GWs practically shuts down after the system of particles settles in the virialized state. The time required to achieve virialization also varies for different configurations with shorter values for t_{vir} resulting in stronger GW emission, something that is expected since smaller timescales mean larger derivatives of the quadrupole moment and therefore increased GW signal.

The total GW signal is an average found only after a sufficiently large number N_{conf} of different configurations is properly considered. We apply a systematic discretization process to scan the continuous spectrum of the parameter space. This requires the repetition of the numerical experiment about $N_{\text{conf}} \sim 5000$ times, each time with different initial conditions. This way we test and record the evolution of N_{conf} initial asphericities dictated by the deformation parameters (α, β, γ) and with a common variance σ . The implementation of such a large number of N -body runs has been made possible by the use of a small computer-cluster. The computational limitations restricted us to consider a relatively small, though seemingly sufficient number of particles $N \sim 10^4$. The total average GW signal obtained can be viewed as a nonlinear superposition of GWs emitted by an assembly of N_{conf} patches each enclosing a perturbation with statistical significance dictated by the Doroshkevich F_D distribution. This averaging procedure yields a GW spectrum characterized by new interesting features. Instead of a single smooth peak, which is given by the Zel'dovich solution, there is a two-peak structure. The extra peak is attributed to the violent relaxation processes that are not captured by the Zel'dovich framework. Actually, hump-like features around the peak appear at the GW spectrum already before the average time of pancake collapse. This is a fine-structure difference compared to the Zel'dovich result and it is understood from the fact that shell-crossing processes do not occur simultaneously in all the configurations. The recognition that there is a specific GW signature of the virialization process on the GW spectrum is one of the main

results of this work.

Our primary interest here is for gravitational collapse processes taking place on scales that enter the Hubble horizon before the big bang nucleosynthesis (BBN), though our results can be applied to processes occurring after recombination as well. The assumption of an EMD era realized before BBN is not standard, however it is common and natural in several Beyond the Standard Model (BSM) set-ups. Actually, the earliest epoch we can confidently gain information about the early Universe is for temperatures $\mathcal{O}(1)$ MeV where BBN takes place [15]. In this aspect GWs account for a unique and very valuable probe, see e.g. [16] for a recent review. For larger energy scales we are ignorant about the energy content of the Universe and only at ultra high energy scales an inflationary stage is postulated. Between the BBN epoch and the Planck or the inflationary era stretches an extensive, in terms of e-folds, cosmic period where a deviation from the steady thermal state (radiation domination (RD)) cannot be excluded. Common examples that can realize an EMD are the slow decay of the inflaton field or the slow decay of massive metastable particles that dominated the total energy density. What is of particular interest is that these fields can naturally realize an EMD era if they act as scalar condensates. Hence, the virialized halo that we observe in our simulations is an ephemeral one that we assume to finally evaporate due to particle decays that reheat the Universe. We will restrict ourselves to an idealized pure EMD era and we will not explore the possible implications of the gradual decay of the condensate.

GWs production during EMD at linear order cosmological perturbation theory has been studied in refs. [17, 18]. At second order in the expansion of cosmological perturbations, tensor perturbations are sourced, dominantly, by quadratic combinations of first-order scalar perturbations [19–21]. The GW amplitude is found to have a strong sensitivity on how fast or slow the transition from EMD to RD is [22]. GWs are also sourced by possible isocurvature perturbations of the fluid component that realizes the EMD, see e.g. [23–26] for GWs from the primordial black hole (PBH) dominated early Universe. An extra motivation to study GW production during EMD is given by several proposals of nonlinear structure formation which is not necessarily washed out by the reheating [27–33]. The limitations of the perturbative analysis due to the presence of a nonlinear scale [34] restricts the applicability of the existing formalism which describes the production of secondary GW during EMD. In this respect, our analysis can be viewed as complementary to the perturbative one adding further insights into particular aspects of the nonlinear processes involved in the gravitational collapse. Earlier studies [35–37] have explored the GW production during an EMD era and within the non-perturbative regime N -body numerical tools were utilized. More recently ref. [38] performed N -body simulations taking into consideration the decay of the matter fluid incorporating the impact of reheating. In our work we give a comparative study between semi-analytic Zel’docivh and the corresponding numerical N -body results and highlight quantitatively the implications of the virialization stage on the GW spectrum.

The second assumption we make is that the amplitude of the power spectrum of primordial curvature perturbations rises at small scales (although our results could be adjusted to the case of a scale invariant spectrum). The minimal assumption is that the spectrum of primordial fluctuations $\mathcal{P}_{\mathcal{R}}(k)$ is nearly flat over a wide range of length scales. Deviations from flatness could have arisen naturally on some small scale if there is a strong feature in the inflaton potential, see e.g. ref. [39] for a recent review. The associated length scale may be far below the scales observed in cosmic structures and correspond to small or even tiny horizon masses. Examples of overdensities with masses of order of magnitude $10^{-21}M_{\odot}$, $10^{-12}M_{\odot}$ and $10M_{\odot}$ will be explicitly discussed. If the power of such a high-wavenumber fluctuation is significant a detectable GW signal can be produced. It is actually exciting that at low frequency bands PTA experiments report a stochastic GW background signal. This signal has already implications on early Universe cosmological scenarios, see e.g. [40–43]. In higher frequency bands, LIGO-Virgo-KAGRA are putting constraints on the amplitude of the background. Additionally to the stochastic GW background, a PBH population in a mass range analogous to that of the overdensity might be produced during EMD [44–51] and contribute to the dark matter in the

Universe. The correlation between the PBH abundance and the associated GW spectrum, see e.g. [52–66] for some recent discussion, is a rather fascinating aspect of this cosmological scenario.

The structure of the paper is as follows. In sec. 2, after a brief introduction to the Zel’dovich approximation, we overview the salient aspects of the N -body numerical techniques. We describe the initial conditions for the density perturbations and the methodology that we follow to run our simulations. In this respect we quote the Doroshkevich PDF which specifies the statistical significance of the initial profile for the shape-fluctuations considered. In sec. 3 we describe the formalism for the computation of the GW spectrum within the quadrupole approximation. We present in detail the dynamics of the N -body distribution and the subtle evolution of the density profile identifying the critical stages. We compute the gravitational radiation emitted during the numerically simulated collapse and we compare it with the previous results obtained within the Zel’dovich (semi)-analytic framework. In sec. 4 we describe the probability sampling method we follow to compute the overall average GW signal. We discuss particular examples of GWs signals that can be potentially detectable by operating or future GW detectors, giving also emphasis to the recent positive results of PTA experiments. We finish in sec. 5 with a discussion and our conclusions.

2 The theoretical set up

In an earlier study [12] we followed the Zel’dovich approximation to describe the nonlinear evolution of the density perturbation and compute the emitted gravitational radiation until the stage of pancake collapse. Our goal in this work is to complement this earlier study by investigating the evolution of the triaxial shapes of various simulated systems until they reach the virialized state and compute the associated GW emission.

We assume that at some cosmic moment t_k a linear density perturbation mode with mass M enters the cosmological horizon. Initially the Hubble flow stretches the linear inhomogeneity with the spatial size growing proportional to the scale factor. The relative amplitude of the linear perturbation grows with its energy density decaying slightly more slowly than that of the background. When the perturbation amplitude reaches unity the linear description is inadequate and a nonlinear description should takeover. At the time labeled t_{\max} the gravitational field created by the perturbation leads to a contraction which overwhelms the Hubble expansion. In the spherical limit this time corresponds to maximal spatial size of the overdensity. For nonspherical configurations it is the moment of the turnaround of one out of three spatial directions.

2.1 Zel’dovich approximation

For pressureless matter the geometrical shapes of realistic inhomogeneities are typically far from spherical and their collapse is strongly anisotropic. At a first approximation the anisotropic collapse can be described by the Zel’dovich solution. This solution describes the nonlinear behavior of a perturbation with arbitrary shape, superimposed on three-dimensional Hubble flow. The relation between the Eulerian r_i and Lagrangian q_i coordinates can be written as [67]

$$r_i = a(t)q_i + b(t)p_i(q_j), \quad (1)$$

where $a(t)$ is the usual scale factor encoding the expansion of the Universe, $b(t)$ is a growing mode associated with the gravitational instability in a pressureless EMD Universe and p_i are deviation vectors that depend on the shape of the initial perturbation. The motion of a group of particles around q_i is described via a deformation (strain) tensor $D_{ij} = \partial r_i / \partial q_j$. After choosing a comoving coordinate system where the matrix $\partial p_i / \partial q_j$ is diagonal

$$\frac{\partial p_i}{\partial q_j} = -\text{diag}(\alpha, \beta, \gamma), \quad (2)$$

it is $D_{ij} = \text{diag}(a - \alpha b, a - \beta b, a - \gamma b)$. All the properties of the deformation tensor are governed by the density-perturbation spectrum.

A perturbation characterized by the size $q = k^{-1}$ enters the horizon at t_k satisfying $a(t_k)q = H_k^{-1}$, where $H_k \equiv H(t_k)$ is the Hubble scale at the time t_k . For simplicity we consider monochromatic perturbation. One can relate the horizon entry time t_k with the mass M contained

$$t_k = \frac{4GM}{3}. \quad (3)$$

We assume initially small deviations from sphericity, $\alpha b(t_k)/a(t_k) \ll 1$, $\beta b(t_k)/a(t_k) \ll 1$, $\gamma b(t_k)/a(t_k) \ll 1$ so that at t_k the triaxial perturbation is nearly inside the Hubble sphere, $r_i(t_k) \approx a(t_k)q$, where \vec{r} is the position of the ellipsoid boundary. At the moment of horizon entry the density contrast field at linear order is

$$\delta_L(t_k) = (\alpha + \beta + \gamma) \frac{b(t_k)}{a(t_k)} \ll 1. \quad (4)$$

During matter domination the density perturbation in the linear regime grows as $\delta \propto a$ and hence $b \propto a^2$. The deformation tensor changes much more rapidly than the Hubble flow factor $a(t)$ and according to eq. (1) a turnaround will occur along one of the three axes. The turnaround direction is identified with r_1 after assuming the hierarchy for the deformation parameters

$$\alpha > 0, \quad -\infty < \gamma \leq \beta \leq \alpha < \infty \quad \text{and} \quad \alpha + \beta + \gamma > 0. \quad (5)$$

Four important moments are identified: the horizon entry t_k , the maximum expansion time t_{max} , the collapse time t_{col} and, for special initial conditions, the black hole formation time t_{BH} . An extra important moment t_{virial} , that signifies the virialization stage, will be introduced in the next subsection. At the moment of maximum expansion the mass is about to shrink, $\dot{r}_1(t_{\text{max}}) = 0$ with the primordial perturbation along r_1 having half of the size compared to the unperturbed expansion, $r_1(t_{\text{max}}) = a(t_{\text{max}})q_1/2$. This is the turnaround radius $r_1(t_{\text{max}})$ at which the expansion halts in this direction and collapse commences. In configurations with spherical symmetry all shells are assumed to have zero velocities at the same time. For non-spherical configurations the turn-around radius is different in every direction. During matter domination it is $a(t) \propto t^{2/3}$ and the ratio $a(t_{\text{max}})/a(t_k)$ yields the following expression for the moment of maximum expansion,

$$t_{\text{max}} = \left(\frac{\alpha + \beta + \gamma}{2\alpha\delta_L(t_k)} \right)^{3/2} t_k. \quad (6)$$

Using Eq. (1) and the fact that $b(t) \propto a^2(t)$, we can write within the analytical approximation (Zel) the evolution of the principal semi-axis of the triaxial ellipsoid as a function of time,

$$r_i^{\text{Zel}}(t, \alpha, \beta, \gamma, \delta_L) = \frac{3}{2} t_k^{1/3} t^{2/3} \left(1 - \frac{\xi_i}{2} \left(\frac{t}{t_{\text{max}}} \right)^{2/3} \right) \quad \text{for } t < t_{\text{col}}, \quad (7)$$

where ξ_i takes the values $\xi_i = \{1, \beta/\alpha, \gamma/\alpha\}$ for the three directions respectively and $t_{\text{max}} = t_{\text{max}}(\alpha, \beta, \gamma, \delta_L)$. For times $t > t_{\text{max}}$ there will be an infalling flux of matter and the perturbation will collapse first in one dimension forming a two dimensional sheet, called Zel'dovich pancakes. The moment that $r_1(t_{\text{col}}) = 0$ it is

$$t_{\text{col}} = 2\sqrt{2} t_{\text{max}}. \quad (8)$$

A normalization for the growing mode is

$$\frac{b(t)}{a(t)} = \frac{a(t)}{a(t_k)} \quad (9)$$

With this normalization choice the density field is $\delta_L = \alpha + \beta + \gamma$ and $t_{\text{max}} = (1/2\alpha)^{3/2} t_k$. Also, the perturbation is a triaxial configuration with axes ratios $1 - \alpha : 1 - \beta : 1 - \gamma$.

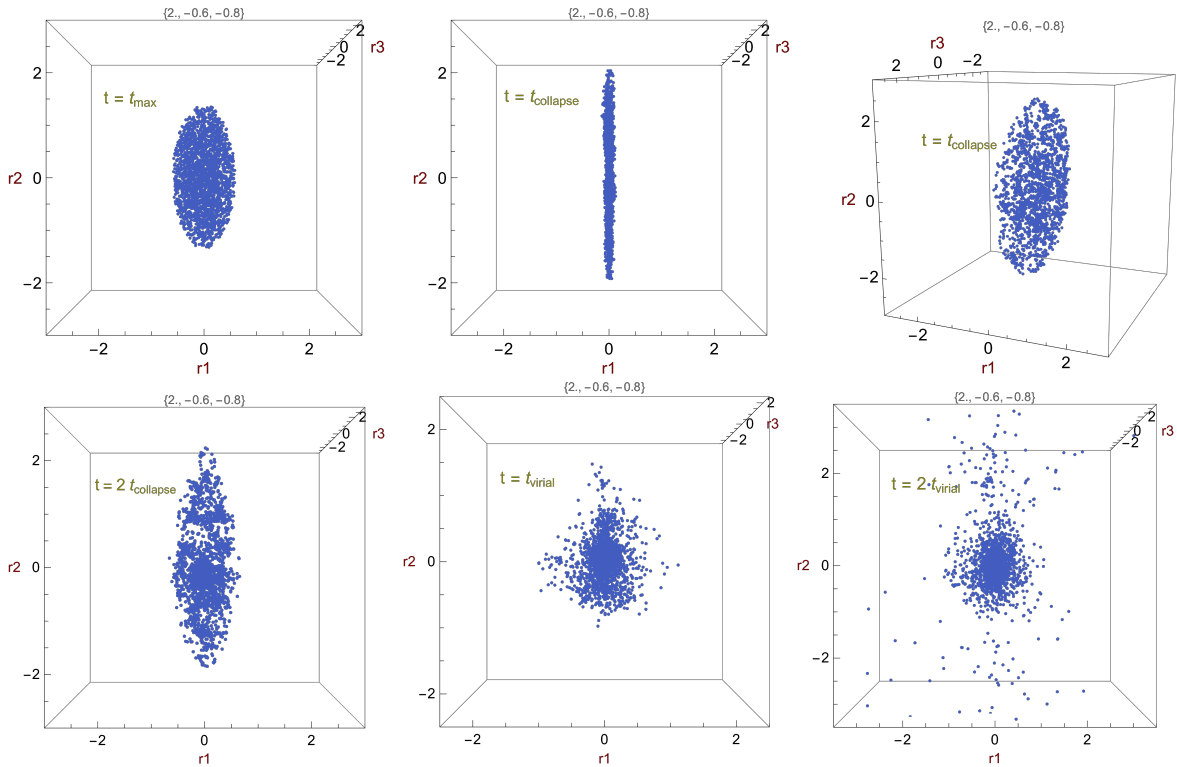


Figure 1: The panels show a projection of the orbits of a cloud of $N = 2500$ particles on the r_1 - r_2 plane for a density perturbation with $\sigma = \sigma_3\sqrt{5} = 0.1$ and deformation parameters $(\alpha/\sigma_3, \beta/\sigma_3, \gamma/\sigma_3) = (2, -0.6, -0.8)$.

From the expressions (7) we see that, within the Zel'dovich approximation, the principal semi-axes of the ellipsoid contract only for $\xi_i > 0$. By definition contraction happens automatically for the r_1 direction because α is positive definite. The other two directions can either collapse, for positive β, γ or expand for negative β, γ . It is however expected that after the formation of the Zel'dovich pancakes the other directions will eventually collapse ending up to a gravitationally compact structure, where the overdensity has reached a certain level. Apparently, the Zel'dovich description gradually fails to track the evolution of the gravitational collapse and eventually breaks down at the stage of the pancake.

2.2 N -body description

The lack of an accurate description of the collapsing process via simple analytic means necessitates the use of N -body numerical tools. The density perturbation can be described by a collection of mass particles with positions and velocities respectively

$$\vec{x}_i(t), \quad \vec{v}_i(t), \quad i = 1, \dots, N \quad (10)$$

where the index i runs over the particles of the distribution. In our set up the dynamics over timescales $t \ll t_{\text{reh}}$ is that of a collisionless system in which the constituent particles move under the influence of the gravitational field generated by the time-varying mass distribution. N -body simulations produce a numerical solution for arbitrary large times and reveal the subtle details of the gravitational collapse. In fig. 1 an animation of the evolution of the particle distribution is displayed in snapshots at the moments of maximum expansion, pancake collapse and finally when the system has settled to approximate equilibrium, called virialization. The moment t_{virial} indicates the initiation of the virialization stage. This moment is identified as a bottleneck stage associated with the evolution of the quadrupoles which we will further discuss in sec. 3. In comparison with the analytic result (7), the simulations show that departures from the analytic description start appearing for times $t > t_{\text{max}}$. These departures might be

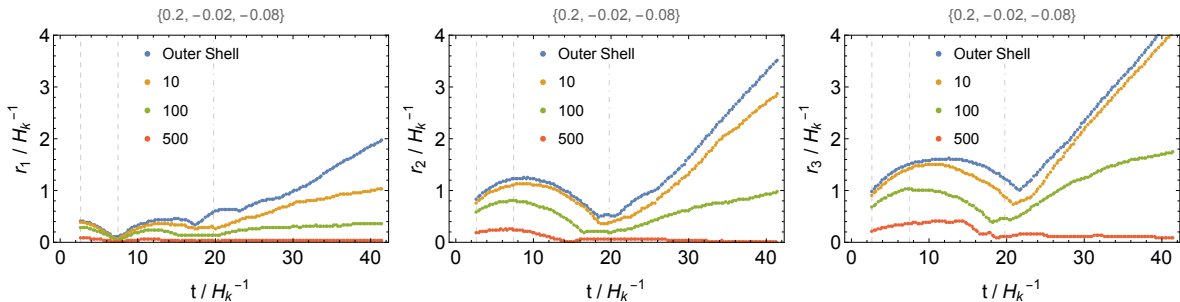


Figure 2: The panels show the evolution of the semi-axes of the outer and three inner one-particle shells (10th, 100nd, 500th) of the N -body distribution in directions r_1, r_2 and r_3 for $\sigma = 0.1$ and deformation parameters $(\alpha, \beta, \gamma) = (0.2, -0.02, -0.08)$.

mild or strong depending on the deformation parameters (α, β, γ) . N -body simulations are particularly valuable for times $t > t_{\text{col}}$, where the analytical solutions (7) are definitely not applicable.

A system of N particles interacting gravitationally with total mass M and a characteristic dimension R reaches a dynamic equilibrium state on a timescale comparable to a few times the typical free fall timescale $t_{\text{ff}} \approx 1/\sqrt{GM/R^3} \sim (G\rho)^{-1/2}$, where ρ is the mass density of the distribution. This is the response time needed to settle down to virial equilibrium, that is

$$\frac{T}{|U|} = 0.5, \quad (11)$$

where $T = \frac{1}{2} \sum_{i=1}^N m_i |\vec{v}_i|^2$ is the kinetic and $U = -\frac{1}{2} \sum_{i \neq j} G m_i m_j / |\vec{x}_i - \vec{x}_j|$ the potential energy of the system. Equation (11) is a statement of the scalar virial theorem. If the system is initially out of equilibrium, virialization is reached through mixing in phase space due to fluctuations of the gravitational potential, a process called violent relaxation [68]. A reasonable approximation is that a spherical distribution virializes at about the same time that this idealized model collapses to a singular density. For anisotropic collapse the simulations show that the virialization time takes longer, about a couple of t_{col} times, see the right plots of fig. 3. After the distribution has settled to approximate equilibrium, its radius can be estimated from the virial theorem. An analytical result exists for a spherical configuration with the half-mass radius of the distribution being about one-third of the turnaround radius. For anisotropic collapse, the results of the simulation show that roughly the same conclusion holds.

The initial conditions for our N -body simulations are critical and we determine them by the Zel'dovich solution. We assume that the Zel'dovich approximation describes sufficiently well the evolution of the overdensity until the moment of maximum expansion t_{max} . After that moment we assume that the overdensity has effectively decoupled from the background and the Hubble flow can be neglected from the gravitational dynamics. We consider the evolution of the overdensity for times $t \geq t_{\text{max}}$ as an effectively cold gravitational collapse and we describe it utilizing the N -body simulations.

We suppose that at some initial time t_k there is a density fluctuation of size k^{-1} and variance $\sigma^2 = \langle \delta_{\perp}^2 \rangle$, with a small initial asphericity described by nonzero values for (α, β, γ) , that enters the Hubble radius. In the framework of N -body simulation the density perturbation is initially composed of an approximately homogeneous distribution of identical N particles. In analogy with eq. (7) the semi-axis of the ellipsoidal particle distribution $r_i^{\text{NB}}(t)$ can be numerically specified. We run the N -body simulation for initial conditions that are set at the moment of the turnaround. Hence, the initial positions $|\vec{r}_{\text{init}}^{\text{NB}}|$ of the particles placed at the boundary of the distribution and along the directions of the principal axes are determined by eq. (7) and (9) for $t = t_{\text{max}}$,

$$r_{1,\text{init}}^{\text{NB}} = \frac{1}{4\alpha} H_k^{-1}, \quad \frac{r_{2,\text{init}}^{\text{NB}}}{r_{1,\text{init}}^{\text{NB}}} = 2 - \frac{\beta}{\alpha}, \quad \frac{r_{3,\text{init}}^{\text{NB}}}{r_{1,\text{init}}^{\text{NB}}} = 2 - \frac{\gamma}{\alpha}. \quad (12)$$

Accordingly, the maximal initial velocities v_i along the directions of the principal axes are

$$v_{1,\text{init}}^{\text{NB}} = 0, \quad v_{2,\text{init}}^{\text{NB}} = \sqrt{2} \frac{\alpha - \beta}{\sqrt{\alpha}}, \quad v_{3,\text{init}}^{\text{NB}} = \sqrt{2} \frac{\alpha - \gamma}{\sqrt{\alpha}}. \quad (13)$$

We study systems with $N \lesssim 10^4$ particles each with equal mass $m_i = M/N$. All systems are initialized by randomly placing particles in an ellipsoid volume with space borders prescribed by the equation $(x/r_{1,\text{init}}^{\text{NB}})^2 + (y/r_{2,\text{init}}^{\text{NB}})^2 + (z/r_{3,\text{init}}^{\text{NB}})^2 = 1$ and radial velocities that increase linearly from zero, in the center of the distribution, to the boundary values given by eq. (13). With these initial conditions, the distribution evolves anisotropically under the influence of the self-gravitational field. In our numerics we set $G = 1$. We calibrate the timescale of the N -body evolution by the timescale t_{max} of Zel'dovich dynamics by fixing the span of N -body evolution from the initial time until the pancake collapse as follows

$$\Delta t_{\text{col}} = (t_{\text{col}} - t_{\text{max}}) \approx 1.8 t_{\text{max}}. \quad (14)$$

This is approximately equal to the free-fall time $\sim (G\rho)^{-1/2}$ for a particle at the position $r_{1,\text{init}}^{\text{NB}} = (3t_{\text{max}}/2)^{2/3}/2$. The mass is assumed to be constant and cold throughout this first stage of collapse, i.e. there is no flow of matter across the shells. The fact that we follow the Zel'dovich approximation until the moment of maximum expansion might introduce a systematic error in our results, which presumably it is a minor one. The advantage of this methodology is that it makes our analysis self-consistent and transparent and any refinement to the overall signal can be consistently carried out.

We numerically track the evolution of the system from the moment of turnaround until times $t_{\text{end}} \gg t_{\text{max}}$ so that the collapse, the violent relaxation and virialization processes take place. Within the time interval $[t_{\text{max}}, t_{\text{end}}]$ we take successive snapshots of the N -body distribution with step $\Delta t_{\text{step}}^{\text{NB}} \ll t_{\text{max}}$. We stop the N -body simulation deep in the virialized regime, where a nearly spherical configuration is formed surrounded by an outflow of particles escaping the gravitational potential, see figs. 1 and 2. We take a common t_{end} value for every configuration $t_{\text{end}} \sim 150 t_k$. Roughly 500 snapshots from t_{max} until the end time t_{end} are sufficient to capture the details of the evolution of the N -body distribution. Those configuration that evolve slowly and virialize later than $150 t_k$, give a negligible contribution to the GW signal. Deviations from Zel'dovich description are observed already at the stage of collapse with the radii of the N -body distributions having much smaller sizes compared to those given by eq. (7),

$$r_2^{\text{NB}}(t_{\text{col}}) < r_2^{\text{Zel}}(t_{\text{col}}), \quad r_3^{\text{NB}}(t_{\text{col}}) < r_3^{\text{Zel}}(t_{\text{col}}). \quad (15)$$

This means that the bulk mass is much more concentrated compared to the Zel'dovich picture at the time of pancake collapse. The deviations decrease for the case where $\gamma \sim \beta \sim \alpha$ where a nearly spherical collapse takes place. Eventually, the Zel'dovich approximation breaks down and for $t \gtrsim t_{\text{col}}$ the N -body simulations reveal the subtle details of the gravitational evolution.

For illustration reasons we choose three benchmark configurations, out of several thousands examined, to explicitly display the evolution of the collapsing distribution, see figs. 3. In these benchmark configurations some of the subtle features in the quadrupole evolution are clearly evident and the deviations from Zel'dovich approximation are manifest. In the left panels of figs. 3 the evolution of the r_i^{NB} is tracked by the particles positioned at the boundary of the distribution along r_1 , r_2 and r_3 directions respectively. The result of the N -body simulation, depicted with dots separated with time step $\Delta t_{\text{step}}^{\text{NB}}$, is compared with the Zel'dovich solution (solid cyan lines). The moments of turnaround and pancake collapse are indicated with dashed gridlines, while the so-called bottleneck stage is indicated with the dot-dashed gridline. At t_{col} and along r_1 direction the Zel'dovich solution is in agreement with the N -body result by construction but in the other two directions there is an apparent discrepancy. In the plot we also see that for $t \gg t_{\text{col}}$ the outermost particles of the distribution finally escape the central concentration. Clustering occurs mainly for inner particles. In the plots the thin dotted blue line, that corresponds to 200th outermost particle along r_1 , illustrates the evolution of an inner

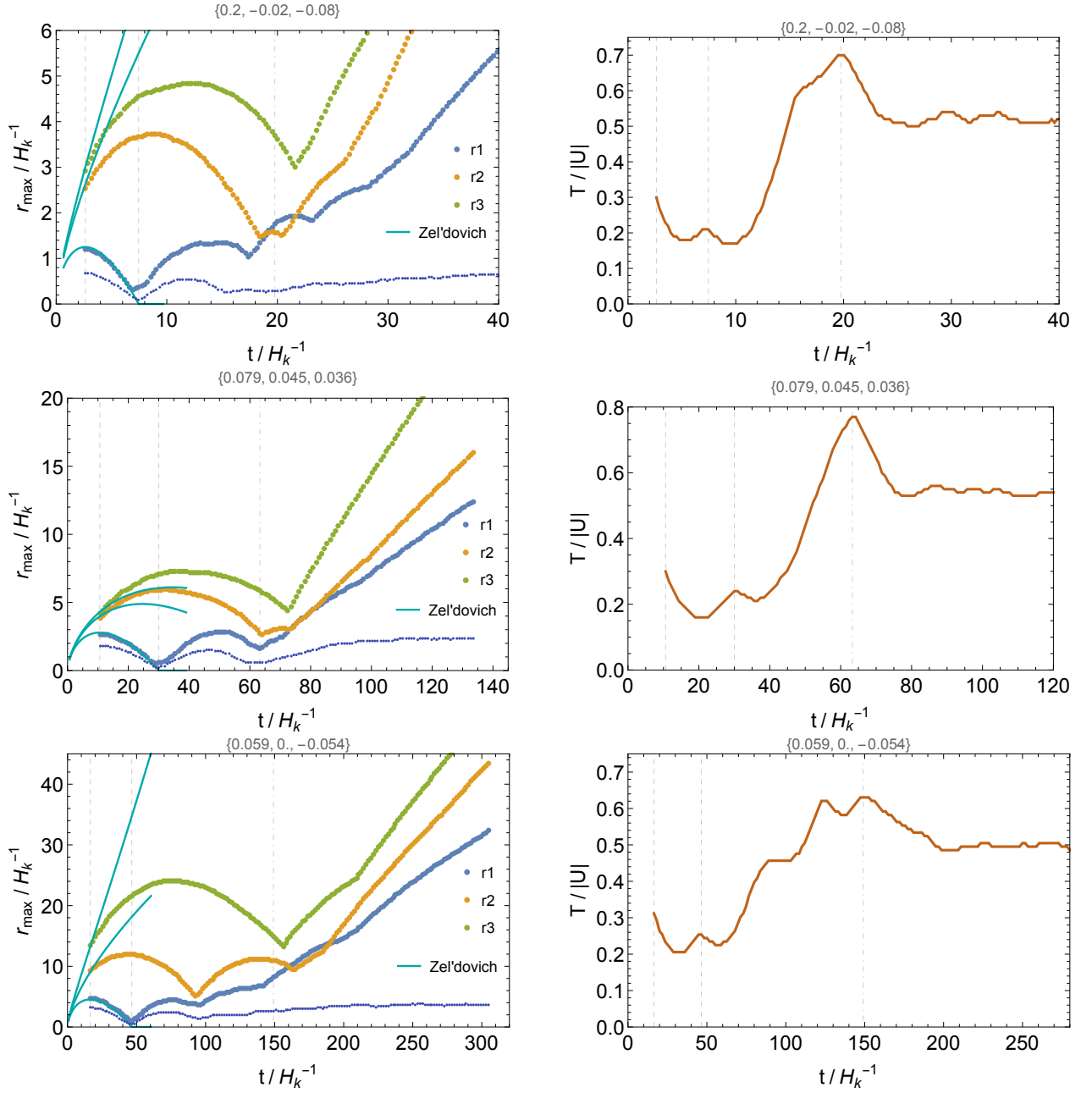


Figure 3: N -body results are displayed for an overdensity with $\sigma = 0.1$ and deformation parameters $(\alpha, \beta, \gamma) = (0.2, -0.02, -0.08)$ (*top panels*), $(0.079, 0.045, 0.036)$ (*middle panels*), $(0.059, 0, -0.054)$ (*bottom panels*) simulated by $N = 2500$ particles. *Left panels*: The coordinate of the outermost particles in the N -body distribution along the directions r_1 , r_2 and r_3 are shown. With the thin dotted blue line the evolution of an inner shell is shown. For comparison the Zel'dovich solution is depicted in cyan lines. *Right panels*: The virial ratio of kinetic over potential energy of the N -body distribution. The gridlines in all the plots denote from left to right the moments of turnaround (t_{\max}), pancake collapse (t_{col}) and the bottleneck stage (t_{virial}).

one-particle shell. The evolution of inner shells is displayed in more detail in fig. 2 where the outflow and inner flow motions are demonstrated.

Our objective is the computation of the average GW energy emitted by a Hubble patch of size k^{-1} that undergoes gravitational collapse and the finding of the total spectrum of GWs propagating in our Universe today. Taking a particular combination of deformation parameters (α, β, γ) is only a case study out of infinite combinations and does not, of course, represent the average GW emission. Actually, the differences in the emissivity of GWs can be extremely large for different values of the deformation parameters. This means that we have to consider a large number of different configurations N_{conf} , each characterized by a unique combination (α, β, γ) , and properly add their gravitational contribution. This is done by considering the Doroshkevich PDF $\mathcal{F}_D(\alpha, \beta, \gamma, \sigma)$ which gives the statistical significance of a perturbation with a specific asphericity.

2.3 Doroshkevich PDF

The average GW signal is the cumulative effect of numerous gravitational sources and has a critical dependence on the statistical properties of the deformation parameters. We assume that the shape-fluctuation defines a three-dimensional random field that follows a Gaussian distribution. For a homogeneous and isotropic background space the probability distribution function for α , β and γ is

$$\mathcal{F}_D(\alpha, \beta, \gamma) d\alpha d\beta d\gamma = -\frac{27}{8\sqrt{5}\pi\sigma_3^6} \times \exp\left[-\frac{3}{5\sigma_3^2} \left((\alpha^2 + \beta^2 + \gamma^2) - \frac{1}{2}(\alpha\beta + \beta\gamma + \gamma\alpha)\right)\right] \times (\alpha - \beta)(\beta - \gamma)(\gamma - \alpha) d\alpha d\beta d\gamma, \quad (16)$$

and is called Doroshkevich PDF [11]. Doroshkevich was the first to apply these methods extensively to the study of the formation of cosmic structure. The σ_3^2 is the dispersion of the diagonal components of D_{ij} . The value σ_3^2 is related to the dispersion of the density perturbations by

$$\sigma^2 \equiv \langle \delta_L^2 \rangle = \int_{-\infty}^{\infty} d\alpha \int_{-\infty}^{\alpha} d\beta \int_{-\infty}^{\beta} d\gamma \mathcal{F}_D(\alpha, \beta, \gamma, \sigma_3) (\alpha + \beta + \gamma)^2 = 5\sigma_3^2. \quad (17)$$

At the early time t_k the density perturbation in each Hubble patch is characterized by a degree of initial asphericity described by the parameters (α, β, γ) of the deformation tensor with distribution of the values given by $\mathcal{F}_D(\alpha, \beta, \gamma, \sigma)$ probability density function (PDF). The probability two principal values of the deformation tensor to be nearly equal ($\alpha \simeq \beta \simeq \gamma$) is particularly small. Extreme values of asphericity are also rare. Along the lines of eq. (17) the quantities $\langle t_{\text{max}} \rangle$ and $\langle t_{\text{col}} \rangle$ can also be found.

The differential number of sources with deformation parameters lying in the range $(\alpha, \alpha + d\alpha)$, $(\beta, \beta + d\beta)$ and $(\gamma, \gamma + d\gamma)$ are

$$dN_{\text{source}} = \frac{\mathcal{H}_0^{-3}}{k^{-3}} \mathcal{F}_D(\alpha, \beta, \gamma, \sigma) d\alpha d\beta d\gamma, \quad (18)$$

where \mathcal{H}_0 is the comoving Hubble parameter today. The Doroshkevich PDF is normalized to unity and integration over the entire parameter space (α, β, γ) gives N_{source} equal to $\mathcal{H}_0^{-3}/k^{-3}$, which is the number of Hubble patches of size $\frac{4}{3}\pi k^{-3}$ enclosed in the comoving volume of the present Universe. Here we are interested in patches that enclose an overdensity hence we restrict ourselves in integration intervals dictated by eqs. (5) and, additionally, by the requirement $t_{\text{max}} \geq t_k$. The last condition reads $\alpha \leq 1/2$ and together with eqs. (5) they define the parameter space of interest \mathcal{S} . The integral $I_D = \int \int \int_{\mathcal{S}} d\alpha d\beta d\gamma \mathcal{F}_D(\alpha, \beta, \gamma, \sigma)$ is to a good approximation equal to $1/2$. Besides the number of sources $\mathcal{H}_0^{-3} k^3 I_D$ we will also consider an ensemble of configurations N_{conf} in order to estimate the average GW signal emitted by a single Hubble patch. The size of N_{conf} is determined by the number of bins with width $\Delta\alpha$, $\Delta\beta$ and $\Delta\gamma$ that span the parameter space \mathcal{S} of possible deformations. We will discuss the significance of N_{conf} and the specification of the optimal number of bins in more detail in sec. 4.

3 The energy density of GWs emitted during gravitational collapse

As the overdensity undergoes rapid compression and collapses under its gravity, the asymmetrical process generates gravitational waves. By studying the properties of the emitted waves we can learn about the presence of possible overdensities, their masses and amplitudes, their nonlinear evolution and probe the history of the early Universe. We estimate the spectrum of GWs emitted from mass distributions that end up to halo formation via N -body simulations. We also compare it with analytic results, that partially describe the collapsing process. We use the quadrupole approximation and assume that the quadrupole moment is the primary source of gravitational radiation, while higher-order moments have significantly weaker contributions.

3.1 Quadrupole approximation

The equation of motion of tensor perturbations to a background of a Friedmann-Robertson-Walker metric in conformal Newtonian gauge is

$$\ddot{h}_{ij} + 3H\dot{h}_{ij} - \frac{\nabla^2}{a^2}h_{ij} = 4S_{ij}^{\text{TT}}, \quad (19)$$

where S_{ij}^{TT} is the source term, the transverse-traceless (TT) part of the anisotropic stress tensor [19–21]. The total gravitational energy radiated is distributed among multipoles of the perturbation $h_{\mu\nu}$. To lowest order in the multipole expansion it is $h_{ij}(t, d) \propto \ddot{Q}_{ij}(t - d/c)/d$, where Q_{ij} is the mass quadrupole moment, d the distance from the source and the overdot denotes time derivative. This formula is valid for any nearly Newtonian slow-motion source. Such sources emit GWs with wavelength larger than the size of the source, that implies internal velocities $v \ll 1$ [69]. In terms of the moment of inertia the quadrupole moment is written as

$$Q_{ij} = -I_{ij}(t) + \frac{1}{3}\delta_{ij}\text{Tr}I(t), \quad (20)$$

where I_{ij} , is the moment of inertia tensor defined as $I_{ij} = \int d^3r \rho(\vec{r}) (\delta_{ij}|\vec{r}|^2 - r_i r_j)$. The anisotropic collapse of the bulk mass of the density perturbation produces gravitational radiation. The power emitted in the form of GWs from a Hubble patch, that encloses a perturbation with a quadrupole tensor Q_{ij} , is

$$\frac{dE_{\text{GW}}}{dt} = \frac{G}{5c^5} \sum_{ij} \ddot{Q}_{ij}(t)\ddot{Q}_{ji}(t). \quad (21)$$

After expanding the quadrupole in Fourier series and taking the continuum limit for ω , where \tilde{Q}_{ij} is the Fourier mode of the quadrupole $Q(t)$, the spectral density of GWs is found to be

$$\frac{dE_{\text{GW}}}{d\ln\omega} = \frac{4\pi G}{5c^5} \omega^7 \sum_{ij} |\tilde{Q}_{ij}(\omega)|^2. \quad (22)$$

Gravitational radiation emitted at time t_e with an energy E_{GW} is today observed with energy $E_{\text{GW}}/(1 + z_e)$ and angular frequency $\omega_0 = \omega/(1 + z_e)$. The cosmological redshift is given by $1 + z_e = a_0/a(t_e)$, where we take $a_0 = 1$. The differential energy density parameter of the stochastic GW background per observed logarithmic frequency $\rho_{\text{crit}}^{-1}d\rho_{\text{GW}}/d\ln\omega$ is given in ref. [12]

$$\Omega_{\text{GW}}(t_0, \omega_0) = \frac{1}{\rho_{\text{crit}}(t_0)} \int \int \int_{\mathcal{S}} d\alpha d\beta d\gamma \frac{1}{1 + z_e} \frac{1}{V_k} \frac{4\pi G}{5c^5} \sum_{ij} |\tilde{Q}_{ij}(\omega)|^2 \omega^7 \mathcal{F}_{\text{D}}(\alpha, \beta, \gamma, \sigma), \quad (23)$$

where the integration takes place over the parameters space of interest \mathcal{S} . $\rho_{\text{crit}}(t_0)$ is the critical energy density of the Universe today and $V_k = 4\pi k^{-3}/3$ is the comoving volume at the time of

horizon entry of the perturbation. In terms of the frequency parameter today f_0 , Eq. (23) is recast via the relation $\omega = 2\pi f_0(1+z_e)$. We will assume that the EMD era transitioned abruptly into RD era at the cosmic time t_{rh} , where the subscript ‘‘rh’’ denotes quantities defined at the moment of reheating. In this case the comoving wavenumber for $k > k_{\text{rh}}$ and the comological redshift are

$$k(M, T_{\text{rh}}) \simeq \left(\frac{3M(1+z_{\text{rh}})^3}{4\pi\rho_{\text{rh}}} \right)^{-1/3}, \quad 1+z_e = \frac{1+z_{\text{rh}}}{(6\pi G\rho_{\text{rh}})^{1/3}} t_e^{-2/3}, \quad (24)$$

where $\rho_{\text{rh}} = \pi^2 g_* T_{\text{rh}}^4/30$ and z_{rh} are respectively the energy density and the redshift at the time of reheating. Otherwise, in the case of a gradual transition from the EMD to RD, there will be deviations from the approximation $w = 0$ and the expansion rate will be different depending on the fractional distribution of the energy density components (as e.g. in the approach of [38]). Here we will focus on the ideal case of cold gravitational collapse which is clear both in the modeling and the simulation level.

The expression (23) is the equation which gives the total average signal produced in a $\Delta t = t - t_k$ time interval during which $\ddot{Q}_{ij}(t) \neq 0$. Finding Q_{ij} is the ultimate objective and we will determine utilizing N -body simulations. For the sake of comparison we will first review the result found in the framework of Zel’dovich approximation [12] in the following subsection.

3.2 GWs computed from the Zel’dovich solution

Within Zel’dovich approximation we get the solutions (7) and the evolution of $Q_{ij}(t)$ can be described analytically for times $t_k \lesssim t \lesssim t_{\text{col}}$. By choosing the principal axes frame, the moment of inertia tensor of the ellipsoid is $I_{ij} = \frac{1}{5}M \text{diag}(r_2^2 + r_3^2, r_1^2 + r_3^2, r_1^2 + r_2^2)$, where M is the total enclosed mass, and the components of the quadrupole are

$$Q_{ij}^{\text{Zel}}(t) = \frac{3M}{80} \left(\frac{t_k}{t_{\text{max}}^2} \right)^{2/3} \frac{1}{\alpha^2} \left[(3c_{ij}^2 - \alpha^2 - \beta^2 - \gamma^2) t^{8/3} - 4(3c_{ij} - \alpha - \beta - \gamma) t^2 t_{\text{max}}^{2/3} \right] \delta_{ij}, \quad (25)$$

where $c_{ij} = \text{diag}(\alpha, \beta, \gamma)$. In particular for a time bin $[t_1, t_2]$ within the $[t_k, t_{\text{col}}]$ interval the analytic expression is found

$$\begin{aligned} \omega^6 \sum_{ij} |\tilde{Q}_{ij}^{\text{Zel}}(\omega)|^2 &= \frac{1}{54\pi^2} \frac{t_k^{4/3} t_1^{4/3}}{t_{\text{max}}^{8/3}} M^2 \left[1 + \left(\frac{\beta}{\alpha} \right)^4 + \left(\frac{\gamma}{\alpha} \right)^4 - \left(\frac{\gamma}{\alpha} \right)^2 - \left(\frac{\beta}{\alpha} \right)^2 \left(1 + \left(\frac{\gamma}{\alpha} \right)^2 \right) \right] \\ &\times \left| \text{Ei} \left[\frac{1}{3}, i\omega t_1 \right] - \left(\frac{t_2}{t_1} \right)^{2/3} \text{Ei} \left[\frac{1}{3}, i\omega t_2 \right] \right|^2. \end{aligned} \quad (26)$$

The above expression makes possible the exact calculation of the integral (23). In Ref. [12] the GW signal is computed for a range of frequencies after a straightforward numerical integration, under the approximation (7) valid for times $t \lesssim t_{\text{col}}$. The only required input is the deviation of the density perturbations at horizon entry in the linear regime, σ , and the characteristic length scale of the density perturbation k^{-1} (or the mass M) which specifies the time of entry t_k .

The spectrum of the emitted energy E_{GW} is given by eq. (22) and involves exponential functions Ei with an argument that depends on time, either the initial t_1 or the final time t_2 , described by eq. (26). One choice is to consider the time interval $(t_1, t_2) = (t_{\text{max}}, t_{\text{col}})$. Another choice it is to take the limit $t_1 \rightarrow t_k$ that gives the quadrupole evolution from the moment of horizon entry. These two choices yield spectra with small differences as one can see in the left panel in fig. 4. At IR frequencies $\omega t_2 \lesssim 1$ the terms $\text{Ei}[1/3, i\omega t_1]$ and $(t_2/t_1)^{2/3} \text{Ei}[1/3, i\omega t_2]$ balance each other and the expression (26) is constant. These imply that the quantity $\omega^7 \sum_{ij} |\tilde{Q}_{ij}^{\text{Zel}}(\omega)|^2$ has a peak at $\omega \sim t_2^{-1}$ with amplitude proportional to $\delta_L^{7/2}/t_k$. In the left panel of fig. 4 four GW spectra are depicted for $H_k = 1$. With dark yellow

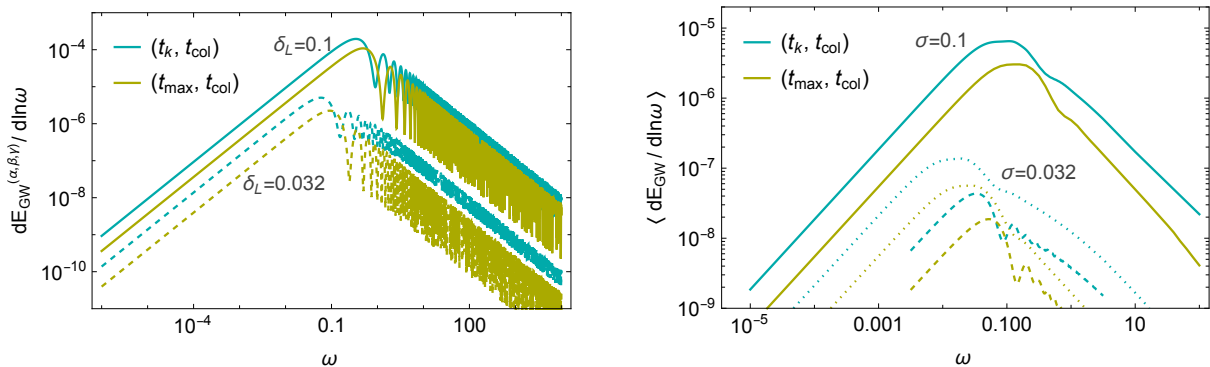


Figure 4: *Left panel:* The Zel'dovich solution for the GW spectrum for a specific example of deformation parameters $(\alpha, \beta, \gamma) = (0.2, -0.02, -0.08)$ (solid lines) and $(0.2/\sqrt{10}, -0.02/\sqrt{10}, -0.08/\sqrt{10})$ (dashed lines) which correspond to $\delta_L = 0.1$ and $\delta_L = 0.032$ respectively. The dark cyan lines are for the interval $(t_1, t_2) = (t_k, t_{\text{col}})$ and dark yellow for $(t_1, t_2) = (t_{\text{max}}, t_{\text{col}})$. *Right Panel:* The average GW spectrum found after integration over the parameter space (α, β, γ) with the constraint $t_{\text{max}} < 50 t_k$ for $\sigma = 0.1$ (solid line) and $\sigma = 0.1/\sqrt{10} \approx 0.032$ (dashed line). The dotted lines correspond to an integration with the constraint $\langle t_{\text{max}} \rangle < 50 t_k$. In the plots we have set $H_k = 1$.

lines the results of ref. [12] are depicted, whereas the dark cyan lines correspond to the choice $(t_1, t_2) = (t_k, t_{\text{col}})$ that we consider in the current analysis.

The average GW energy emitted is given, within the Zel'dovich approximation, by the integral

$$\left\langle \frac{dE_{\text{GW}}^{\text{Zel}}}{d \ln \omega} \right\rangle = \int \int \int_{\mathcal{S}} d\alpha d\beta d\gamma \frac{4\pi G}{5c^5} \omega^7 |\tilde{Q}_{ij}^{\text{Zel}}(\omega)|^2 \mathcal{F}_{\text{D}}(\alpha, \beta, \gamma, \sigma_3). \quad (27)$$

The exact value of the peak depends on the interval of integration $\alpha_{\text{min}} < \alpha < 1/2$. By taking smaller α_{min} values the amplitude of the average GW spectrum receives contributions from configurations with slow evolution and the amplitude of the spectrum increases, particularly in the infrared frequency range, see fig. 5. For the limiting case that $\alpha_{\text{min}} \rightarrow 0$ configuration that experience a turnaround at infinite times are also counted. Because of the finite duration of the EMD phase we consider α_{min} values which give $t_{\text{max}} < 10^2 t_k$ or $\alpha > 0.023$. For larger values for α_{min} an oscillatory pattern appears in the ultraviolet regime of the spectrum, see the bottom curve in fig. 5. This can be understood by the fact that larger α_{min} limits the spread of t_{max} values and consequently it operates as a time-filter selecting configurations which evolve in more synchronized manner. Equivalently, the oscillatory pattern also appears by keeping α_{min} constant but decreasing the σ value. For $t_{\text{max}} < 10^2 t_k$ we attain the plots depicted in the right panel of fig. 4. The spectrum peaks at the angular frequency $\omega_{\text{peak}} \sim t_{\text{col}}^{-1}$ with maximum amplitude $\sim 8 \times 10^{-6}$ for $\sigma = 0.1$ and having set $H_k = 1$. By decreasing σ the amplitude of the spectrum decreases in a way that depends on the parameter space of integration \mathcal{S} . If the ratio t_{max}/t_k is kept fixed while σ gets smaller the ensemble of configurations with a significant PDF value shrinks, which changes both the amplitude and the shape of the spectrum (depicted with dashed lines in the r.h.s. of fig. 4). If instead we decrease σ but keep the σ -dependent ratio $\langle t_{\text{max}} \rangle / t_k$ fixed, the shape of the spectrum nearly does not alter: it decreases roughly as $\sigma^{7/2}$ with the peak shifting at smaller frequencies according to the relation $\omega_{\text{peak}} \propto \sigma^{3/2}$ (dotted lines in the r.h.s. of fig. 4).

The expression (27) gives the average GW power at the time of emission from a perturbation of an arbitrary mass. In order to find the signal received in the present Universe a mass scale for the overdensity and T_{rh} have to be specified. The differential energy density parameter of the stochastic GW background Ω_{GW} can be computed after choosing values for the reheating

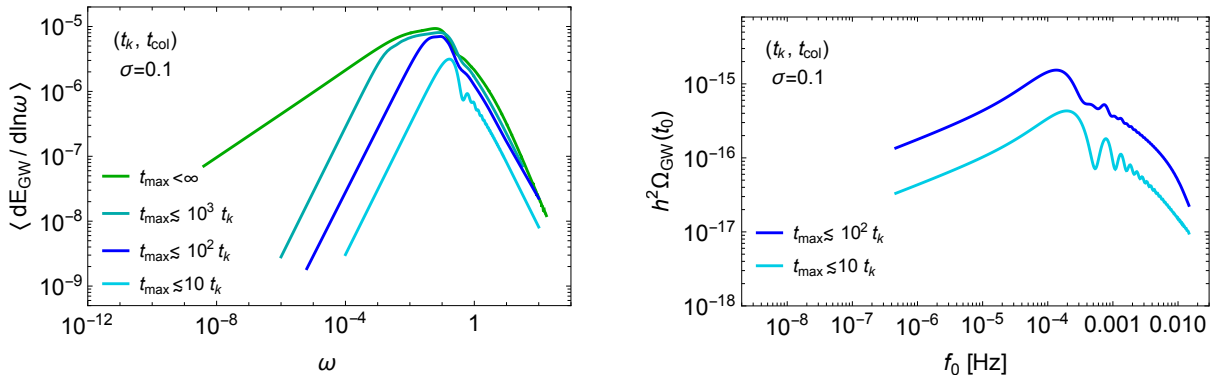


Figure 5: *Left panel:* The average GW power emitted from configurations that experience a turnaround at $t_{\text{max}} \lesssim 10t_k$, $t_{\text{max}} \lesssim 10^2t_k$, $t_{\text{max}} \lesssim 10^3t_k$ respectively from the bottom to the top. The upper curve is the power emitted for arbitrary large times including configurations that turnaround at cosmologically non-viable times. *Right Panel:* The corresponding differential energy density parameter in the present Universe $\Omega_{\text{GW}}(t_0, f_0)$ for $M = 10^{-12}M_{\odot}$ and $T_{\text{rh}} = 1$ GeV.

temperature T_{rh} and the mass M of the perturbation:

$$\Omega_{\text{GW}}^{\text{Zel}}(t_0, f_0) = \frac{2^4}{30 \times 54} \frac{g_s(T_0) T_0^3}{\rho_{\text{crit}}(t_0)} \frac{4\pi G}{5c^5} M T_{\text{rh}} \omega_0 \times \int \int \int_{\mathcal{S}} (\alpha^4 + \beta^4 + \gamma^4 - \alpha^2\beta^2 - \alpha^2\gamma^2 - \beta^2\gamma^2) \times \left| \text{Ei} \left[\frac{1}{3}, i\omega_0(1+z_e)t_k \right] - \left(\frac{t_{\text{col}}}{t_k} \right)^{2/3} \text{Ei} \left[\frac{1}{3}, i\omega_0(1+z_e)t_{\text{col}} \right] \right|^2 \mathcal{F}_{\text{D}}(\alpha, \beta, \gamma, \sigma). \quad (28)$$

In the above expression we took $(t_1, t_2) = (t_k, t_{\text{col}})$ and the redshift parameter at the time of collapse $1+z_e = 1+z(t_{\text{col}})$. For benchmark values $M = 10^{22}$ g, $T_{\text{rh}} = 10^3$ GeV at the frequency value $\omega_0/2\pi = 1$ Hz the coefficient in front of the integral is 4×10^{-6} .

The expression (28) has been derived following closely the methodology established in [12]. In that work the results were presented for the time interval $(t_1, t_2) = (t_{\text{max}}, t_{\text{col}})$ and after making a simplification, for the sake of numerical efficiency, to approximate δ_{L} with the dispersion σ in the integrand. That choice gave spectra close to the exact ones for large σ values. The expression (28) is exact and it is written for $(t_1, t_2) = (t_k, t_{\text{col}})$. The overall sensitivity of the GW amplitude on the σ value is found to be $\Omega_{\text{GW}}(f_0, t_0) \propto \sigma^{7/2}$. In terms of the power spectrum of the curvature perturbations, $\mathcal{P}_{\mathcal{R}}(k) \equiv A_s \sim \sigma^2$, where a peak around k is assumed, the scaling reads $\Omega_{\text{GW}}(f_0, t_0) \propto A_s^{7/4}$. We note that our analytic result, derived within the Zel'dovich and quadrupole approximation, has a scaling in agreement with that reported in ref. [38]. However a comprehensive comparison is not straightforward since our result originates from a monochromatic source and not from a k -band of a scale invariant power spectrum $\mathcal{P}_{\mathcal{R}}(k)$.

3.3 GWs computed from N -body simulations

For times beyond the stage of pancake collapse $t \gtrsim t_{\text{col}}$ the use of N -body simulation is necessary for the qualitative and quantitative description of the evolution of the overdensity. But also for times $t \leq t_{\text{col}}$ the validity of the analytic result (26) gradually attenuates. Utilizing an N -body simulation we proceed beyond the Zel'dovich approximation and examine the evolution of the collapsing matter distribution. According to the analytic expressions (22) and (23), the numerical tracking of the quadrupoles is the essential objective for the computation of the GW emission. The finding of \ddot{Q}_{ij} makes possible the evaluation of the total amplitude and spectrum of the GW field produced during the entire stage of the gravitational collapse.

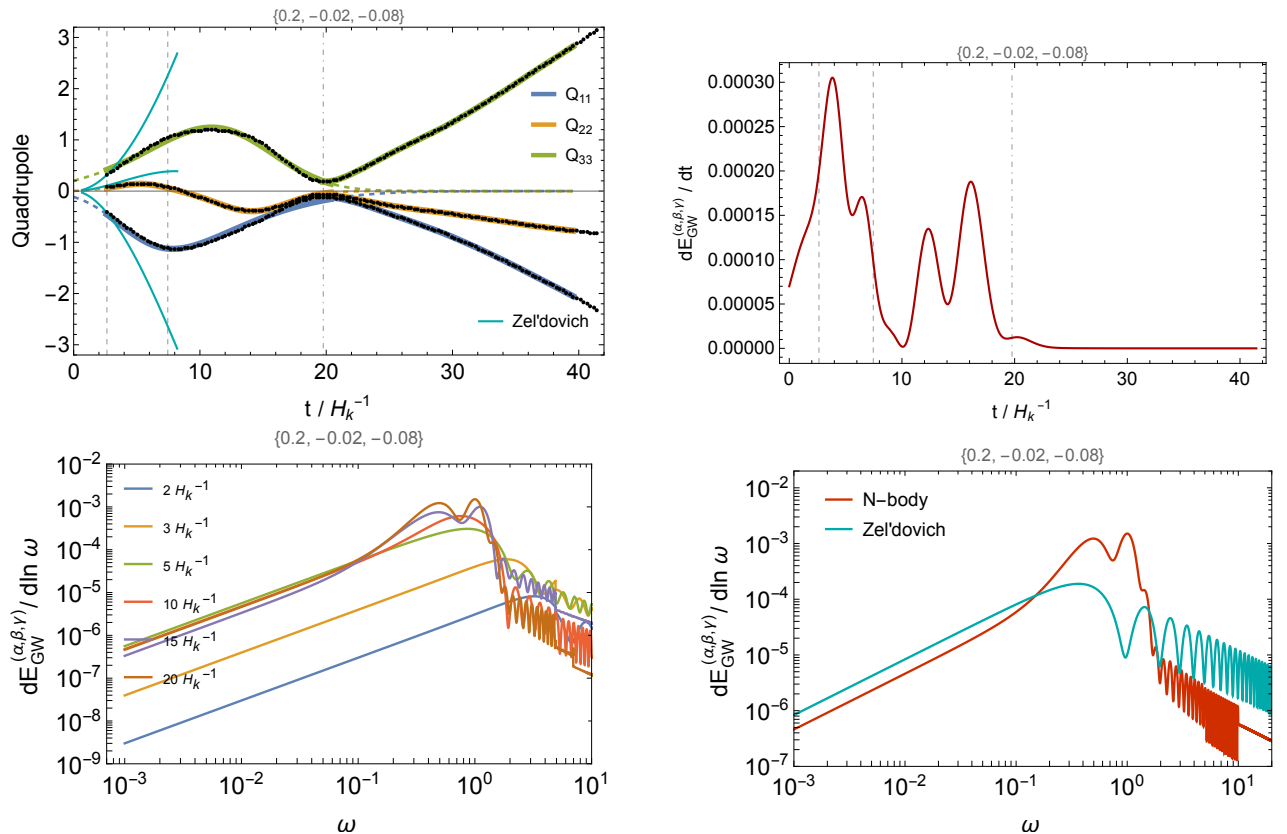


Figure 6: N -body results are displayed for an overdensity with deformation parameters $(\alpha, \beta, \gamma) = (0.2, -0.02, -0.08)$ simulated with $N = 2500$ particles. *Top left panel:* The evolution of the diagonal components of the quadrupole tensor are depicted with black dots. The fitting curves are depicted with blue, orange and green lines. The Zel'dovich solution is depicted in cyan lines. The gridlines from left to right denote the moments of turnaround, pancake collapse and bottleneck stage, in the first two plots. *Top right panel:* The time evolution of the GW power emitted from the Hubble patch. *Bottom left panel:* The spectrum of GWs for different ending t_{end} moments. *Bottom right panel:* Comparison of the spectra of GWs found within Zel'dovich approximation until the moment of pancake collapse and from N -body simulation until virialization.

3.3.1 The evolution of the quadrupole

Gravitational radiation is produced during collapse with power given by eq. (21). The critical quantity is the quadrupole (20) and the moment of inertia for the N -body distribution which is given by the expression

$$I_{ij} = \sum_{n=1}^N m_n \left(|\vec{x}_n|^2 \delta_{ij} - x_i^{(n)} x_j^{(n)} \right). \quad (29)$$

For specific (α, β, γ) values the quadrupole is successively measured in discrete moments t_i in units of H_k^{-1} separated by a step $\Delta t_{\text{step}}^{\text{NB}}$, small enough to give sufficient resolution and track the subtle changes over time. The change of the quadrupole and the GW generation is displayed in figs. 6 - 8 for the three configurations presented in fig. 3. Of special interest is the fact that the quadrupole evolution of these configurations gives off efficiently gravitational radiation. They represent three different types of quadrupole evolution which produce different shapes for the GW spectrum with a notably, strong enhancement compared to the Zel'dovich result. However, they also share common features, generic for all configurations, that we describe next. In the top left panels the result of the N -body simulations for the diagonal $Q_{ij}(t)$ values are depicted with black dots. We note that non-diagonal components of the quadrupole arise and

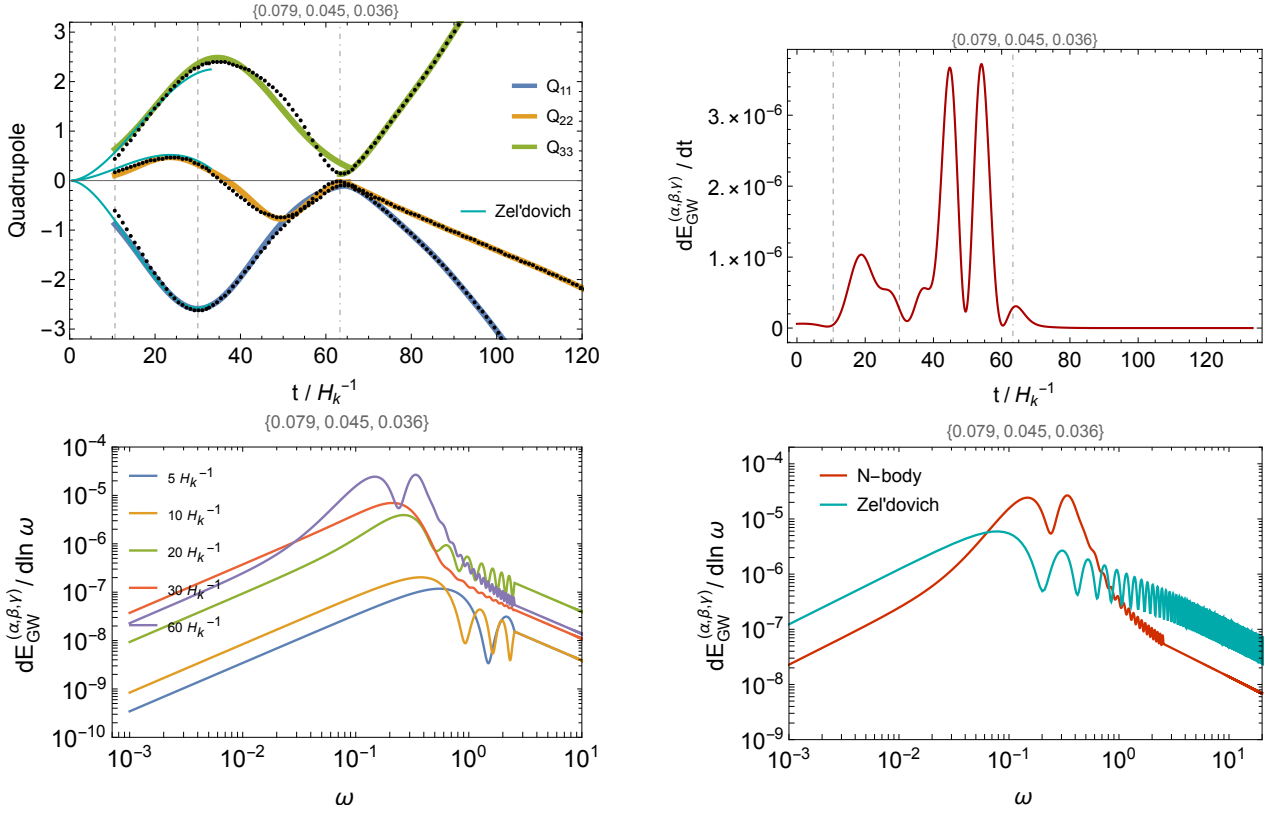


Figure 7: As in fig. 6 for deformation parameters $(\alpha, \beta, \gamma) = (0.079, 0.045, 0.036)$.

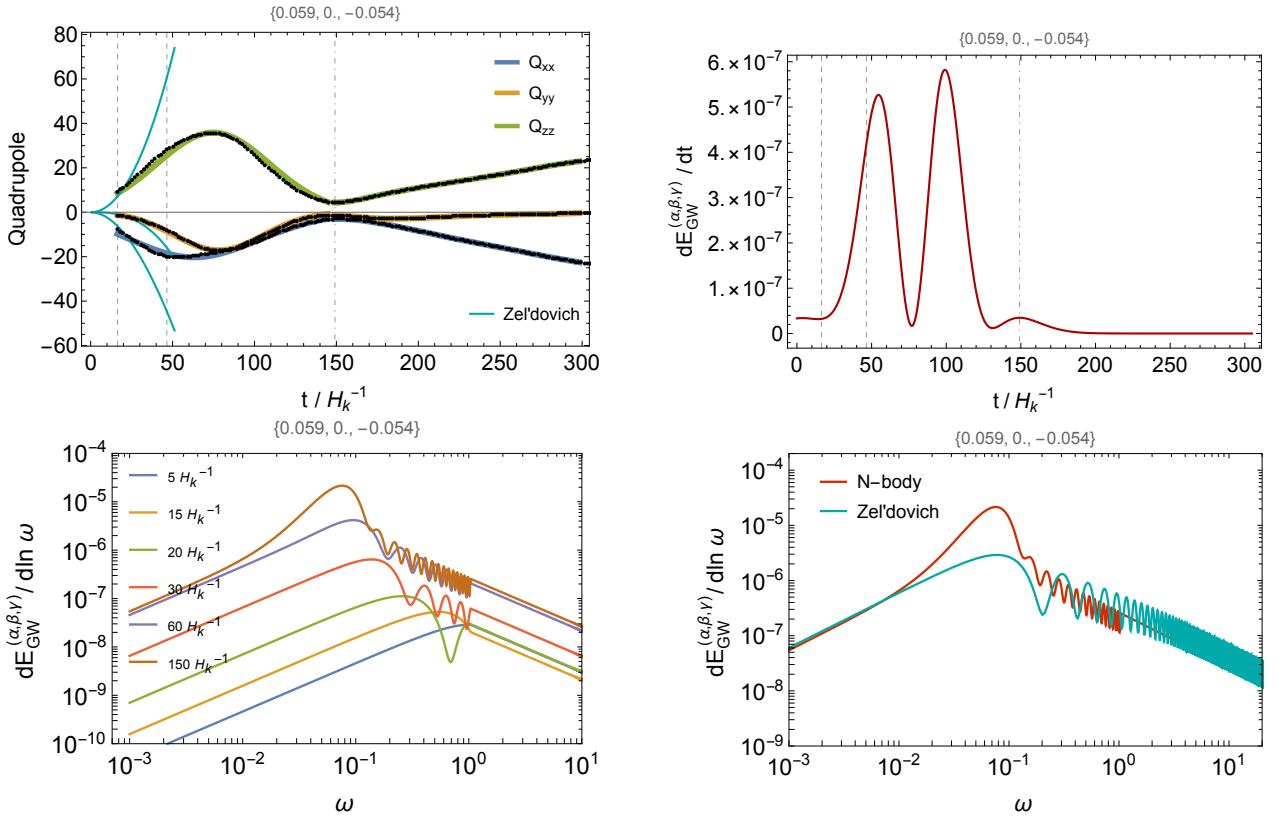


Figure 8: As in fig. 6 for deformation parameters $(\alpha, \beta, \gamma) = (0.059, 0, -0.054)$.

are taken into account, but are not displayed because they are generally about two orders of magnitude smaller than the diagonal ones. Exception are the cases of nearly spherical collapse where the quadrupole components become comparable.

Apart from the distinct stages of turnaround and pancake collapse, particular phases of the quadrupole evolution can be read off the graphical form of the $Q_{ij}(t)$ discrete data:

1. The first phase of the quadrupole evolution is characterized by a skewed bell-shaped curve that takes positive or negative values along the time axis $t > t_k$. The diagonal terms are $Q_{ii} \sim M(2r_i^2 - r_j^2 - r_k^2)$ with $i \neq j \neq k$ and the hierarchy of (α, β, γ) implies that Q_{11} is generally negative, Q_{33} is generally positive, while the sign of Q_{22} is contingent on how small or large the β parameter is with respect to α and γ . An oscillation between positive and negative values is observed in the $Q_{22}(t)$ component for a particular combination of (α, β, γ) parameters. During the first stage of the quadrupole evolution the turnaround, the pancake collapse and shell crossing processes take place in succession. The latter process might cause a flip of sign also for Q_{11} and Q_{33} components, which is visible in particular configurations.
2. The second phase of the quadrupole evolution is characterized by a bottleneck-like shape. During this phase, indicated by the moment t_{virial} , a second collapse occurs and the distribution settles into the virialized state. It is characterized by a minimum value for each $|Q_{ii}(t)|$ diagonal component so that the three of them together form a bottleneck shape that corresponds to a time of maximal contraction. The ratio $T/|U|$ maximizes before it reaches the virial value $1/2$, as displayed in fig. 3. The snapshot of the distribution at the moment t_{virial} is displayed in fig. 1.
3. The third phase of the quadrupole evolution is characterized by a roughly monotonic evolution. This is the final phase of virialization where the ratio of the total kinetic and potential energies are stabilized to the value $K \approx -U/2$. During this stage the $|Q_{ii}(t)|$ values increase steadily because of the moment of inertia carried away by the escaping particles. It is the stage where the GW emission shuts down.

3.3.2 The computation of the emitted GW power

The computation of the GW power requires finding the third time derivatives of the quadrupoles. Successive application of numerical derivatives on the discrete data generally introduces artificial noise. The method we follow to tackle this issue and avoid a possible overestimation is to fit the quadrupole data with suitable functions. In particular, the quadrupole data that span the time interval from t_{max} until the bottleneck stage, are fitted sufficiently well with a skew-normal distribution

$$Q_{ii}(t) \approx \frac{1}{\sqrt{2\pi}\hat{\delta}_i} e^{-\frac{(t-\hat{\mu}_i)^2}{2\hat{\delta}_i^2}} \text{Erfc} \left[-\frac{\hat{b}_i(t-\hat{\mu}_i)}{\sqrt{2}\hat{\delta}_i} \right], \quad (30)$$

with mean value $\hat{\mu} + \sqrt{\frac{2}{\pi}} \hat{b}\hat{\delta}/\sqrt{1+\hat{b}^2}$ and variance $\hat{\delta}^2(1-2\hat{b}^2/(\pi(1+\hat{b}^2)))$. This kind of fitting functions appears to be appropriate for the diagonal quadrupole terms, which are the dominant terms of the tensor Q_{ij} . For the non-diagonal terms, which generally give a subleading contribution, we apply a polynomial fitting. Polynomial functions are also applied to fit the data during the last stage, where virialization has been established. Overall, the compound fitting allows a smooth and reliable evaluation of $\ddot{Q}_{ij}(t)$ from the time of entry t_k until the end of the virialization stage t_{virial} . The fitting functions are depicted with thick blue, orange and green lines over the discrete data for the Q_{11} , Q_{22} and Q_{33} components respectively and displayed in the top left panel of figs. 6 - 8. For comparison the quadrupole derived from the Zel'dovich solution is also displayed truncated at $t \sim t_{\text{col}}$. We see that, in general, a firm analytic description of $Q_{ij}(t)$ within the Zel'dovich approximation exists only for times well before t_{col} .

The gravitational power emitted $\dot{E}_e \sim |\ddot{Q}(t)|^2$ from a Hubble patch that encloses a density perturbation exhibits a very different growth profile for different deformation parameters (α, β, γ) and σ . In the right top panels of figs. 6 - 8, we see that pumps of GW energy density take place at different moments for different configurations from the initial time of turnaround, the stage of pancake collapse and until the establishment of virialization. After the pancake collapse, the system gradually faster or slower, transforms into a virialized state with a spherical core. The virialization procedure involves geometrical changes that might be abrupt with non-axisymmetric mass flow producing a strong GW emission. This is especially evident when the geometry of the bulk mass of the distribution changes from oblate to prolate-like shapes and vice versa. Such changes are manifest from the evolution of the quadrupole component $Q_{22}(t) \sim M(2r_2^2 - r_1^2 - r_3^2)$ which fluctuates about the zero value for particular configurations, with the positive (negative) Q_{22} values corresponding to mostly oblate (prolate) shapes, see the top left panel of figs. 6 and 7. A prolate-oblate geometrical change of the mass distribution is very well captured by our fitting procedure and yields an enhanced GW radiation. In the latter example the quadrupole change is rather acute and a very strong GW emission takes place. When no oscillatory pattern is observed for the quadrupole components the total amount of the GW production is found to be of the same order of magnitude with the GWs produced within the (t_k, t_{col}) time interval. For configurations with symmetric bell-shaped graphical forms for all the $Q_{ii}(t)$ components, the power of the gravitational radiation is characterized roughly by a unimodal distribution as displayed, for example, in the top left panel of fig. 8.

Having specified the entire time evolution of the quadrupole the computation of the spectral density of the gravitational radiation is carried out. The Fourier transform of the third time derivative of the quadrupole,

$$\tilde{Q}_{ij}^{(3)}(\omega) = \frac{1}{2\pi} \int \ddot{Q}_{ij}(t) e^{-i\omega t} dt \quad (31)$$

gives the spectral GW power after using the identity $|\tilde{Q}_{ij}^{(3)}(\omega)|^2 = \omega^6 |Q_{ij}(\omega)|^2$. We implicitly assume a non-vanishing quadrupole only for times between the horizon entry of the perturbation and the reheating of the Universe, i.e. in the time interval $t_k < t < t_{\text{reh}}$. The time of reheating is a free parameter and affects essentially the amplitude and the spectrum of the final GW signal. An early reheating would imply a GW signal produced only from the very first stages of gravitational collapse, while a slow reheating implies that gravitational radiation is produced throughout the collapsing and clustering process. Hence, for $t_{\text{vir}} < t_{\text{reh}}$ the final GW signal is sensitive to the entire dynamics involved in the virialization of the distribution. To make the dependence on the reheating time manifest, we compute the final GW signal for different time intervals $[t_k, t_n]$ after parametrizing the reheating time as $t_{\text{reh}} \sim t_n = nH_k^{-1}$ for positive integers n . In figs. 6-8 the gradual increase of the amplitude of the spectrum $dE_{\text{GW}}/d\ln\omega$ is displayed for increasing t_n values.

In the last panel of figs. 6-8 we display the N -body result for the GW power emitted for $t_{\text{vir}} < t_{\text{reh}}$ together with the GW power computed from the Zel'dovich approximation in the time interval $[t_k, t_{\text{col}}]$. Apparently the entire GW amplitude is larger because of the inclusion of the virialization. Violent relaxation processes that drive the system to a virialized state contribute to $\ddot{Q}(t)$ and the GW emission is enhanced, occasionally significantly, given that reheating occurs after the second collapse or, equivalently, after the bottleneck stage. For reheating times after the establishment of the virialization the emission power practically remains unchanged with the different reheating times affecting only the redshift that the propagating GWs experience.

We note that an early reheating could change the composition of the system and the evolution of the quadrupoles. To avoid the complexities of interacting fluid dynamics we restrict ourselves to the discussion of the dynamics of collisionless matter. When a final state of a virialized spherical distribution is reached we expect that the reheating leaves the predictions for the GW production unmodified.

	Integration	$\alpha \leq \sigma_3$	$\alpha \leq 2\sigma_3$	$\alpha \leq 3\sigma_3$	$\alpha \leq 4\sigma_3$	$\alpha \leq 5\sigma_3$
I_D	1/2	0.05	0.34	0.46	0.49	0.50
$\langle \delta_L^2 \rangle / \sigma^2$	1	0.01	0.35	0.85	0.98	0.99
$\langle t_{\max} \rangle \frac{\sigma^{3/2}}{t_k}$	-	0.08	0.26	0.29	0.31	0.32
N_{conf}	∞	78	650	2191	5267	10395

Table 1: The values of the I_D , $\langle a \rangle$ and $\sigma^{3/2} \langle t_{\max} \rangle / t_k$ are listed obtained after integration over the parameter space \mathcal{S} and after discrete summation for $\sigma_3^2 = 2 \times 10^{-3}$ (or $\sigma = 0.1$). The summation results quoted are for five intervals $\alpha/\sigma_3 \leq 1, 2, 3, 4, 5$ all discretized by a common step $0.2\sigma_3$. The corresponding number of configurations N_{conf} is also listed.

	Integration	$\alpha \leq \sigma_3$	$\alpha \leq 2\sigma_3$	$\alpha \leq 3\sigma_3$	$\alpha \leq 4\sigma_3$	$\alpha \leq 5\sigma_3$
I_D	1/2	0.05	0.35	0.49	0.49	0.50
$\langle \delta_L^2 \rangle / \sigma^2$	1	0.01	0.35	0.85	0.98	0.99
$\langle t_{\max} \rangle \frac{\sigma^{3/2}}{t_k}$	-	0.08	0.26	0.30	0.31	0.31
N_{conf}	∞	80	652	2277	5292	10550

Table 2: As in table 1 but for a variance ten times smaller $\sigma_3^2 = 2 \times 10^{-4}$ (or $\sigma \approx 0.032$).

4 The average GW signal from gravitational collapse

4.1 Probability sampling of configurations

The expectation value of the GW signal is the weighted infinite sum of configurations that continuously span the parameter space of (α, β, γ) , that is an integral over the domain \mathcal{S} given by eq. (23). N -body simulations produce discrete results which correspond to particular configurations. Hence, we estimate the integral (23) numerically applying a probability sampling. We divide each interval in α , β and γ directions in regular sub-interval pieces and appropriately sum the pieces together. The accuracy of the approximation of the breaking of the integral into a sum of pieces depends on the size of the interval considered and the number of steps taken to cross this interval. An adequately large size of the interval is indicated by the probability density function $\mathcal{F}_D(\alpha, \beta, \gamma)$ which decreases exponentially to minute values for $\alpha \gg \sigma_3$. The size of the step $\Delta\alpha$ has to be small enough $\Delta\alpha \ll \sigma_3$ to achieve a sufficient resolution and not surpass configurations that might yield a strong signal. Nonetheless, the size of the step cannot be taken too small because of computational limitations in time and resources.

A ruler for a reliable choice of the interval and step sizes for the discrete sum can be found from the expectation values of quantities that can be precisely computed via straightforward integration. We first consider three pilot examples: the volume I_D of the Doroshkevich PDF in the interval \mathcal{S} (that we referred in sec. 2.3), the expectation values of the sum deformation parameter $(\alpha + \beta + \gamma)^2 = \delta_L^2$ (17) and the turnaround time t_{\max} ,

$$\langle t_{\max} \rangle = t_k \int_0^{1/2} d\alpha \int_{-\infty}^{\alpha} d\beta \int_{-\infty}^{\beta} d\gamma d\alpha d\beta d\gamma \mathcal{F}_D(\alpha, \beta, \gamma, \sigma_3) \left(\frac{1}{2\alpha} \right)^{3/2}. \quad (32)$$

In tables 1 and 2 we list the exact and five approximate values for I_D , $\langle \delta_L^2 \rangle$ and $\langle t_{\max} \rangle$ given by integration and by a discretized summation respectively. The integration interval is the entire parameter space \mathcal{S} while for the discretized summation we consider five different intervals for the positive parameter α which are: $\alpha \leq \sigma_3$, $\alpha \leq 2\sigma_3$, $\alpha \leq 3\sigma_3$, $\alpha \leq 4\sigma_3$ and $\alpha \leq 5\sigma_3$. For each α -interval the corresponding β - and γ -intervals are dictated by the bounds (5). The step-size that spans the three-dimensional interval is $\Delta\alpha = \Delta\beta = \Delta\gamma = 0.2\sigma_3$, which is a choice found to give a sufficient resolution. In table 1 we take $\sigma_3^2 = 2 \times 10^{-3}$ (or $\sigma = 0.1$) for the variance of the Doroshkevich PDF. In table 2 we take $\sigma_3^2 = 2 \times 10^{-4}$ (or $\sigma \simeq 0.032$). The values listed in the tables show that the discretized summation over the interval $\alpha \leq 4\sigma_3$ approximates very well the exact values. The corresponding number of configurations are $N_{\text{conf}} = 5267$ for $\sigma = 0.1$

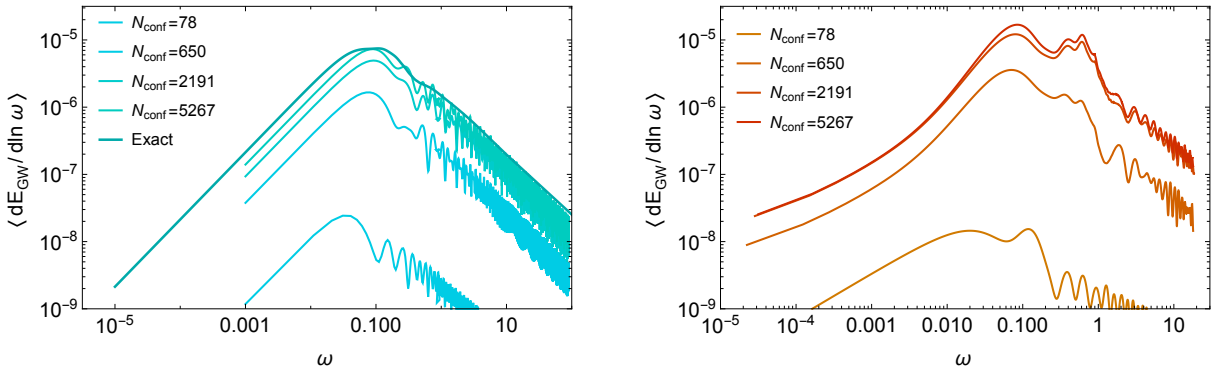


Figure 9: *Left panel:* The progressive convergence of the GW spectra produced within the Zel'dovich description from a discrete summation of N_{conf} configuration is displayed. The exact average result found from integration is also depicted. *Right Panel:* The GW spectra produced from a discrete summation of GW spectra found after running the N -body simulation for N_{conf} different initial conditions are displayed. The plots are for $\sigma = 0.1$.

and $N_{\text{conf}} = 5329$ for $\sigma = 0.032$. Decreasing the size of the step to $\Delta\alpha = 0.1$ would increase N_{conf} an order of magnitude without significantly improving the precision of the results.

Having specified a reliable choice for the sizes of the interval and the step, i.e. $\alpha \leq 4\sigma_3$ and $\Delta\alpha = \Delta\beta = \Delta\gamma = 0.2\sigma_3$ respectively, we proceed with the calculation of the power of the gravitational radiation produced. In this respect we approximate the integral with a discretized summation

$$\begin{aligned} \left\langle \frac{dE_{\text{GW}}}{d\ln \omega} \right\rangle &= \int \int \int_{\mathcal{S}} d\alpha d\beta d\gamma \frac{4\pi G}{5c^5} \omega |\tilde{Q}_{ij}^{(3)}(\omega)|^2 \mathcal{F}_{\text{D}}(\alpha, \beta, \gamma, \sigma_3) \\ &\approx \frac{4\pi G}{5c^5} \omega \sum_{\alpha_i} \sum_{\beta_i} \sum_{\gamma_i} \Delta\alpha_i \Delta\beta_i \Delta\gamma_i |\tilde{Q}_{ij}^{(3)}(\omega, \alpha_i, \beta_i, \gamma_i, \sigma_3)|^2 \mathcal{F}_{\text{D}}(\alpha_i, \beta_i, \gamma_i, \sigma_3). \end{aligned} \quad (33)$$

Contrary to the examples listed in tables 1 and 2 the calculation of (33) is a rather elaborated procedure. It involves N_{conf} runs for the N -body simulation with initial conditions $(\alpha_i, \beta_i, \gamma_i, \sigma_3)$ followed by the necessary data analysis for the finding of the quadrupole and its Fourier modes $\tilde{Q}_{ij}(\omega)$. The repetition of the runs and data analysis for N_{conf} times increases significantly the computational cost. For the computation-intensive purposes of the project we utilized a small cluster of ten computers. Restricting ourselves to a computation that takes time less than a couple of months puts a limitation to the number of particles in our N -body simulations. A large N increases the run-time of the N -body simulations and, moreover, overloads the data analysis. For $N = \mathcal{O}(10^4)$ particles and sufficiently small step $\Delta_{\text{step}}^{\text{NB}}$ and large t_{end} a single simulation takes time $\mathcal{O}(10)$ min and the data analysis several hours. We choose $N = 2500$ after having checked that by varying this value by a couple of times there are no qualitative changes to the amplitude and evolution of the quadrupole.

The average value for the GW signal found after a discrete weighted sum of $N_{\text{conf}} \sim 5267$ different configurations for $\sigma = 0.1$ is expected to approach very well the actual one. This is supported in part from tests of average values of single-valued quantities listed in tables 1 and 2. A second important test is provided by the comparison of the Zel'dovich solution with that produced from the discrete summation. The l.h.s. of eq. (33) can be computed exactly within the Zel'dovich approximation (26) and within the time interval $[t_k, t_{\text{col}}]$. In the left panel of fig. 9 we display the progressive convergence of the summation result and the analytic one with increasing N_{conf} . For the summation and the analytic result we considered configurations that experience a turnaround at times $t_{\text{max}} < 10^2 t_k$ that is for $\alpha > 0.023$. The importance of this test is that it exhibits the convergence of the summation procedure (r.h.s. of eq. (33)) at the exact result (l.h.s. of eq. (33)) for a continuous range of values that span five orders of magnitude in angular frequencies. We note that for smaller α values, $\alpha \lesssim 0.02$ the analytic result would differ in the infrared frequency range, as demonstrated in fig. 5. In this case a

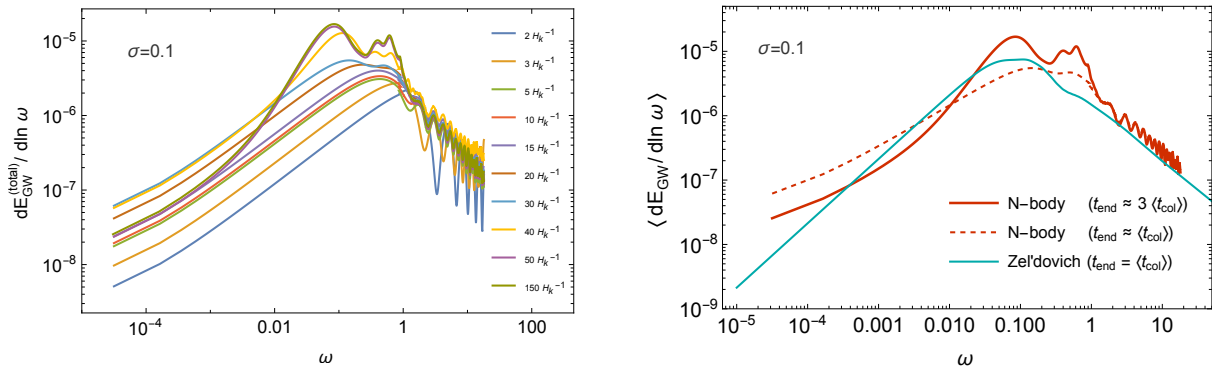


Figure 10: Results of the average GW spectrum (22) for $\sigma = 0.1$. In the *left panel* we display the gradual growth of the GW spectrum as the collapsing process evolves. In the plot legends the corresponding truncation time of the quadrupole evolution can be read off in Hubble time units. In the *right panel* the averaged GW spectrum for the particular times $t_{\text{end}} = \langle t_{\text{col}} \rangle$ and $t_{\text{end}} = 3 \langle t_{\text{col}} \rangle$ are depicted. For comparison the average Zel'dovich spectrum is depicted with the cyan line.

step of a smaller size would be required for an accurate summation procedure.

4.2 The average spectrum of GWs

The aforementioned tests solidify the dependability of our methodology and we can firmly proceed to the estimation of the average power of the gravitational radiation. In the right panel of fig. 9 the average spectrum of GWs is displayed after running the N -body simulation for increasing N_{conf} number. The displayed spectra are approximations of the spectrum of GWs emitted from the moment of entry of the overdensity t_k until a final moment $t_{\text{end}} \gg t_{\text{col}}$ that virialization has been established. For the time interval $[t_k, t_{\text{end}}]$ the tensor $Q_{ij}(t, \alpha_i, \beta_i, \gamma_i)$ is found and the gravitational power emitted is computed from the r.h.s. of eq. (33). A minimum number of configurations is required for a solid result. For $N_{\text{conf}} \lesssim 100$ the summation fails to capture the precise form and the amplitude of the spectrum because configurations with significant contributions are omitted. For $N_{\text{conf}} \gtrsim 2000$ the fine details of the GW spectrum are revealed. The average GW spectrum features an additional peak after the inclusion of the virialization process. The first peak is shaped by the stages of turnaround, pancake collapse and the return to the nearly spherical shape. The peak at higher frequencies is presumably associated with the violent relaxation processes that involve shell crossings and redistribution of the particles. The two peak structure in the spectrum appear after the proper superposition of N_{conf} individual spectra, each with a different peak structure, see figs. 6-8 .

In fig. 10 the average GW spectrum is displayed in a time-lapse sequence. The Q_{ij} evolution is truncated at different moments. The truncation reveals step by step the effects of the virialization process. It can be also viewed as reheating times under the assumption that reheating does not modify the spectrum significantly. Hence, the reheating time and the peak structure are correlated and can specify the reheating temperature. In the left panel, the lower and upper curves are respectively the spectra of GWs emitted within 2 Hubble and 150 Hubble times after the entry of the overdensity. The gravitational radiation gradually increases as the evolution of the gravitational system crosses the stages of pancake collapse and violent relaxation. We also see that after 50 Hubble times the signal has reached its maximum value and its multi-peaked structure has emerged. After that time the form of the spectrum settles into a time-invariant shape. Although there are configurations that continue to give off GWs after $\sim 50 H_k^{-1}$ their contributions to the total spectrum is negligible. The GW signal is dominated by those configurations which evolve fast and source a sizable \ddot{Q}_{ij} .

In the right panel of fig. 10 we display the average GW spectrum at the average moment

of pancake collapse,

$$\langle t_{\text{col}} \rangle = 2\sqrt{2} \langle t_{\text{max}} \rangle \approx 0.9 \sigma^{-3/2} t_k. \quad (34)$$

It is $\langle t_{\text{col}} \rangle \sim 28H_k^{-1}$ for $\sigma = 0.1$. At the time $\langle t_{\text{col}} \rangle$ the structure of the spectrum is characterized by a broad single peak, in quite good agreement with the Zel'dovich result which is also displayed for comparison. However, hump-like features around the peak also appear which originate from shell-crossing processes occurring in configurations that evolve faster than the average and have gone through the pancake collapse phase earlier on. Within $3\langle t_{\text{col}} \rangle$ the average GW spectrum has already attained its final form. It is characterized by a first peak at $\omega_{\text{peak}} \sim H_k/10$ and a second peak, with roughly one half the amplitude, positioned at the angular frequency $\omega_{\text{peak}} \sim H_k/2$ for $\sigma = 0.1$.

The amplitude of the spectrum first peak, found with N -body simulations, is given approximately by the expression, $\langle dE_{\text{GW}}/d\ln\omega \rangle \sim 2 \times 10^{-5}$ for $\sigma = 0.1$. For smaller σ values the spectrum changes according to the discussion in sec. 3.2. Also, the scaling of $\langle dE_{\text{GW}}/d\ln\omega \rangle$ with frequency is $\omega^{3/2}$ at the infrared part of the spectrum and ω^{-1} in the ultraviolet.

4.3 The observable GW signal

The observable GW signal is given by eq. (23). It is determined after three input parameters are specified: the mass M of the perturbations, the deviation σ and the reheating temperature T_{rh} . We will assume here that the time of reheating is late enough for the virialization procedure to complete, i.e. $t_{\text{rh}} \gtrsim 3\langle t_{\text{col}} \rangle$. The amplitude of the observable spectrum about the peak is

$$\Omega_{\text{GW}}(t_0)|_{\text{peak}} \sim 10^{-6} \sigma^{7/2} \left(\frac{M}{M_{\odot}} \right)^{2/3} \left(\frac{T_{\text{rh}}}{\text{GeV}} \right)^{4/3}, \quad (35)$$

where M_{\odot} the solar mass. The spectrum features two peaks which stand out: one broad at frequency given by the expression $f_{\text{peak}} \sim 4 \times 10^{-9} (M/M_{\odot})^{-1/3} (T_{\text{rh}}/\text{GeV})^{1/3}$ Hz and one ruffled peak at frequencies $\sim 5f_{\text{peak}}$. We note that if the power spectrum of curvature perturbations $\mathcal{P}_{\mathcal{R}}(k)$ is (nearly) scale invariant, instead of being enhanced around a particular scale k with corresponding horizon mass M , the characteristic frequency is determined by the reheating temperature T_{rh} .

The differential energy density parameter of the stochastic GW background can be optimistically detected by GW experiments that we describe next. $\Omega_{\text{GW}}(t_0, f_0)$ is constrained from above from BBN/ CMB constraints [70, 71]. It is also indirectly constrained from the PBH production rate associated with the gravitational collapse, see e.g. [2] for a review. A maximal σ value maximizes both Ω_{GW} and the PBH abundance. We recall that the PBH fractional abundance, $f_{\text{PBH}} \equiv \Omega_{\text{PBH}}/\Omega_{\text{DM}}$, is $f_{\text{PBH}} \sim 10^{19} \gamma_{\text{M}} \beta_{\text{PBH}} (T_{\text{rh}}/10^{10} \text{GeV})$. β_{PBH} is the PBH production rate which is given by the expression $\beta_{\text{PBH}} \approx 0.056\sigma^5$ during EMD and for large σ values [46]. We note that the PBH mass does not coincide but is a fraction of the horizon mass $M_{\text{PBH}} = \gamma_{\text{M}} M$. The GW signal can be strong enough to be detectable and possibly discriminated.

We choose three benchmark frequency bands to display the spectrum of the observed GWs. These are the regions of hertz-kilohertz, millihertz and nanohertz where operating or designed GW experiments have an increased sensitivity. LIGO-Virgo-KAGRA [72–74] and Einstein telescope [75], which are ground based interferometers, are sensitive at $10–10^3$ Hz. Space-based designed interferometers LISA [76], Taiji [77], Tianqin [78], Decigo [79, 80], Big Bang Observer (BBO) [81] and μAres [82] are mostly sensitive at $10^{-6}–10^{-1}$ Hz. Pulsar Timing Arrays (PTAs) experiments are sensitive at $10^{-9}–10^{-7}$ Hz. At this low frequency range a measurement of a stochastic GW background is reported by NANOGrav collaboration [83–85], EPTA and InPTA [86–89], PPTA [90–92] and CPTA [93]. These experiments detect a stochastic GW background signal with approximate amplitude of around $h^2 \Omega_{\text{GW}} \sim 10^{-8}$ at the frequency $f \sim 10^{-8}$ Hz. In that frequency rang SKA [94] experiment will also operate. In figs. 11 - 12 we display GW spectra that can be probed by the aforementioned experiments and are produced by specific examples of gravitational collapse that we describe next.

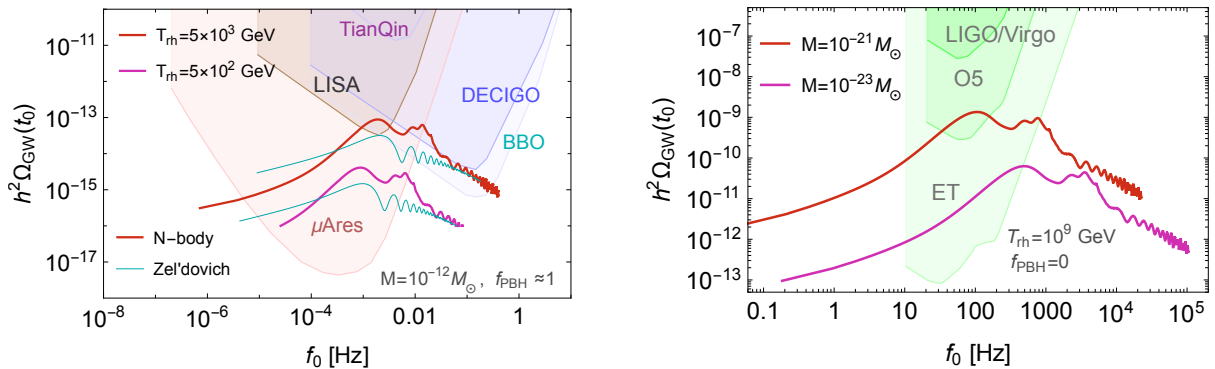


Figure 11: *Left panel:* GW spectra within the LISA-BBO frequency band that are associated with maximal PBH abundance $f_{\text{PBH}} \sim 1$ and horizon mass $M = 10^{-12} M_{\odot}$. With reddish lines the N -body result is displayed and with cyan lines, for comparison, the Zel'dovich result. The upper red line is for $\sigma = 0.01$ and $T_{\text{rh}} \simeq 5 \times 10^3$ GeV and the lower purple line is for $T_{\text{rh}} = 5 \times 10^2$ GeV. *Right Panel:* The GWs associated with promptly evaporating PBHs for $\sigma = 0.1$ and $T_{\text{rh}} = 10^9$ GeV.

- In the left panel of fig. 11 we focus on density perturbations at a mass scale that can be probed by LISA experiment. We assume a maximal σ value which yields PBHs that saturate the dark matter density, i.e. $f_{\text{PBH}} \sim 1$, and have mass $M_{\text{PBH}} = 10^{-12} \gamma_{\text{M}} M_{\odot}$. We also assume $\gamma_{\text{M}} \sim 0.1$ in order to maximize the GW signal (allowing smaller γ_{M} values the GW signal increases significantly). The gravitational collapse yields a GW signal that can be inside the LISA sensitivity curve. In the same plot we consider two different reheating temperatures to stress the T_{rh} dependence: The GW spectra have peaks at different frequency values due to the different expansion history that they experience. Hence, in the event of GW detection the reheating temperature of the Universe can be also probed. If additionally a PBH counterpart is detected the determination of T_{rh} can be a robust result. For comparison, the Zel'dovich result (28) is shown in the plot.
- In the right panel of fig. 11 we focus on the LIGO-Virgo-KAGRA frequency band. The corresponding mass scale is rather small, $M_{\text{PBH}}/\gamma_{\text{M}} \sim 10^{-20} M_{\odot} (T_{\text{rh}}/10^9 \text{ GeV})(f_0/100 \text{ Hz})^3$ and PBH possibly produced are expected to evaporate in the early Universe. An EMD era at such high energy scales is motivated by the slow reheating of the inflaton field. We choose $T_{\text{rh}} = 10^9$ GeV that is realized in scenarios where the inflaton decays gravitationally. We also take $\sigma = 0.1$ and consider two perturbation mass scales: $M = 3 \times 10^{-21}$ and $M = 3 \times 10^{-23}$. We also consider $\gamma_{\text{M}} \ll 1$ so that PBH explosions occur fast enough to evade the BBN constraints [2]. Although $f_{\text{PBH}} = 0$ due to Hawking evaporation, PBH remnants may contribute to the DM density in the Universe, see e.g. [95–100]. We see that the GW signal is well inside the sensitivity curve of Einstein telescope, as well the advanced LIGO-Virgo. It is interesting that LIGO-Virgo already poses constraints and upper bounds on stochastic GW background and PBHs scenarios. Alternatively, (weak) constraints on the reheating temperature of the Universe after inflation can be derived.
- Fig. 12 is about PTA experiments. In that frequency range there is accumulative evidence that a stochastic GW background exists with a significant amplitude. In the plot we have placed the first Fourier bins posteriors of the common EPTA and InPTA signal, represented by the orange violin areas [86] and the NANOGrav signal in gray [85]. Two GW spectra are plotted which are produced by two different overdensities: the first has mass $M = 10 M_{\odot}$ and the second $M = 2.5 M_{\odot}$ for $\sigma = 0.03$. Each GW signal is associated with a PBH population with $f_{\text{PBH}} \approx 10^{-2} \gamma_{\text{M}}$. The horizon masses are rather large and a late reheating is necessary in this scenario. We take $T_{\text{rh}} = 10$ MeV. We see that GWs that originate from gravitational collapse in an EMD Universe could contribute to the observed signal. The particular examples presented can fit better the lowest frequency

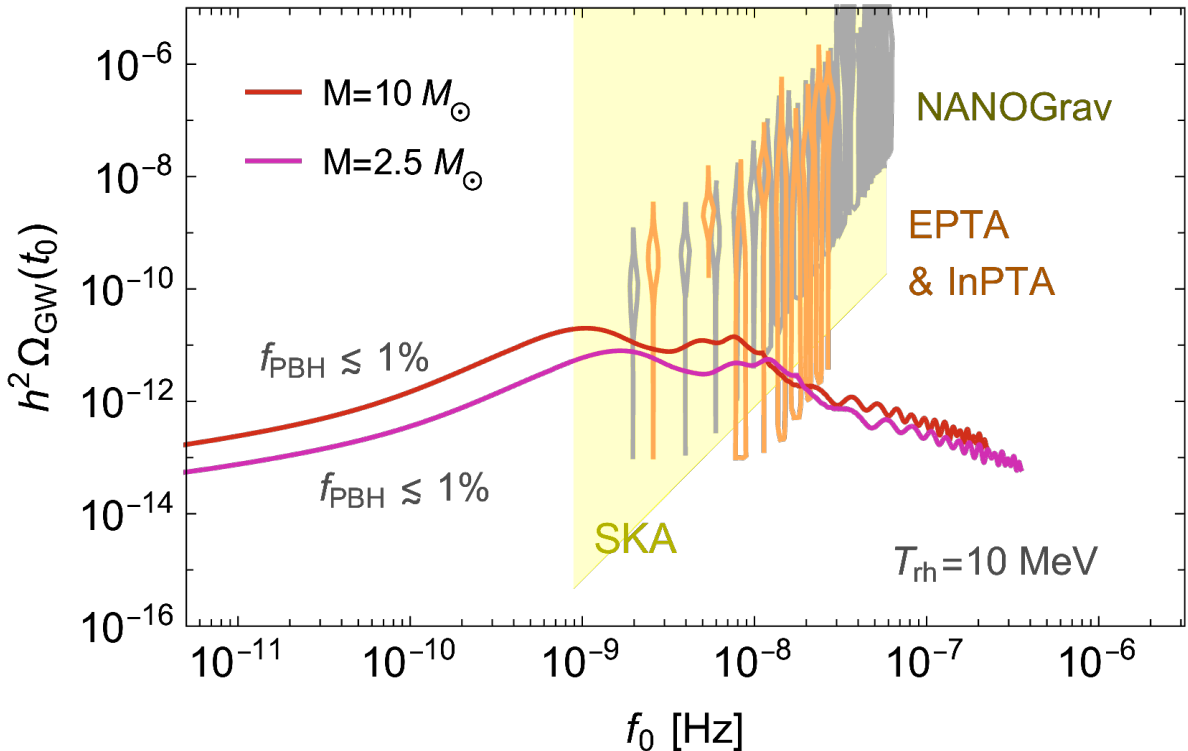


Figure 12: The GW spectrum in the PTA frequency range, for horizon mass $M = 10M_{\odot}$ (red line) and $M = 2.5M_{\odot}$ (purple line) and for $\sigma = 0.03$. The GW signal is associated with a PBH population with fractional abundance $f_{\text{PBH}} \approx 10^{-2}\gamma_{\text{M}}$. The reheating temperature is taken to be 10 MeV. The violins in gray show the posteriors from NANOGrav [85] and in orange from EPTA and InPTA [86].

bins. Fully explaining the observed PTA signal is constrained by the bounds on the PBH abundance.

The detection and identification of the properties and origin of a stochastic GW background is certainly challenging, nevertheless, as we exemplified, a comprehensive understanding of the gravitational collapse can give distinct predictions and informative constraints.

5 Conclusions

In this work we studied the evolution of matter anisotropic gravitational collapse and the associated GW emission via the use of N -body simulations. The great advantage of N -body simulations is that they reveal the evolution of the mass distribution all the way to and beyond the pancake collapse stage. The pancake stage is the limit of validity for the approximate solutions found within the Zel'dovich framework, which were used to compute the GW spectrum in a preceding work [12]. Through N -body techniques, insights into subsequent stages during which the clustering action of gravity becomes manifest, are attained. The full evolution of perturbations from the moment the inhomogeneity drops out of the Hubble flow until the stage of halo formation is traced. The evolution involves anisotropic mass motions, compression and virialization processes which source gravitational radiation.

The total energy radiated is distributed among multipoles and we consider that the dominant contribution comes from the system's quadrupole moment. Density perturbations with different geometric profiles have a different GW emissivity with stronger gravitational radiation arising from large density perturbations with acute aspherical profile. Depending on the initial degree of asphericity the resulting spectrum of the produced GWs might display a single peak, similar to that found within the Zel'dovich approximation, or display an extra peak attributed

to processes occurring during the virialization stage which Zel'dovich approximation cannot capture since it eventually breaks down. Each N -body run simulates the evolution of a particular configurations. In order to find the average GW signal produced by a Hubble patch, we perform a survey of a large number $N_{\text{conf}} \sim 5000$ of configurations that span the space of the different deformation possibilities with a sufficiently small discrete step. This is implemented after N_{conf} runs of the N -body simulation each time with appropriate initial conditions. The resulting GW signal is a superposition of all the configurations. In the averaging procedure we consider the Doroshkevich probability density function, invoking a Gaussian distribution for the shape deformations for the overdensities. The final spectrum displays a two peak structure, with a rough second peak, which reflects the dynamics of virialization processes.

In this work we postulated that a pressureless gravitational collapse has been realized in the very early Universe. A motivation for such postulation is that the GW signal produced could be within the detection sensitivity region of current or designed GW experiments. A significant PBH population associated with the GW signal could be also produced and contribute to the dark matter density. A detection event of such a GW signal would have, among others, two important consequences. First, valuable insights into the virialization dynamics would be gained. Second, it would be a window into the early Universe cosmic history. It would support the realization of an EMD phase, during which deviations from spherical symmetry can significantly grow, and it would provide additional evidence for the presence of BSM physics. In our analysis we did not specify any underlying mechanism that realizes an EMD era but we remained agnostic and we let the reheating temperature to vary. A detection event would also probe the primordial spectrum of curvature perturbations which should not remain scale-invariant within the entire momentum range. This last would also have important implications for the inflationary model building directions.

Our result has been produced by a cold-collapse simulation which uses Newtonian dynamics. The cost of neglecting relativistic effects likely introduces an error of order $(v/c)^2$ which is typically negligible except when the system is near its gravitational radius. In this respect we also assume that the effect of the radiation back-reaction is unimportant, which is justified by the size of $dE/dt \ll 1$. We presume that our results will not change if the number of particles of our N -body simulations increases by several orders of magnitude, i.e. beyond our computational capability. We remark that the initial conditions for the N -body simulations are given by the Zel'dovich solutions at the moment of the turnaround. This choice, though it might introduce a systematic but presumably minor error in our results, it makes possible a consistent analysis of a large collection of vastly different initial configurations. Special attention was paid in the fitting procedure for the components of the quadrupole tensor, in which our result has an increased sensitivity. We also comment that we considered a collisionless collapse, neglecting for simplicity any effect coming from decays and the subsequent reheating of the Universe. A next research step could be to improve upon these issues.

In conclusion, our study advances our understanding of certain aspects of the gravitational collapse in a (early) matter domination era. Ultimately, it is exciting that the sensitivity and the variety of GW detectors increases and we can expect that predicted gravitational signals from primordial Universe can be tested probing the very early Universe and its evolution from the Big Bang till today.

Acknowledgments

ID would like to thank Maria Chira for her assistance with the N -body simulations. ID acknowledges support by the Cyprus Research and Innovation Foundation grant EXCELLENCE/0421/0362.

References

- [1] C. W. Misner, K. S. Thorne and J. A. Wheeler, “Gravitation,” W. H. Freeman, 1973, ISBN 978-0-7167-0344-0, 978-0-691-17779-3
- [2] B. Carr, K. Kohri, Y. Sendouda and J. Yokoyama, “Constraints on primordial black holes,” Rept. Prog. Phys. **84** (2021) no.11, 116902 [[\[astro-ph.CO\]/2002.12778](#)].
- [3] B. Carr, T. Tenkanen and V. Vaskonen, “Primordial black holes from inflaton and spectator field perturbations in a matter-dominated era,” Phys. Rev. D **96** (2017) no.6, 063507 [[\[astro-ph.CO\]/1706.03746](#)].
- [4] I. Dalianis, “Constraints on the curvature power spectrum from primordial black hole evaporation,” JCAP **08** (2019), 032 [[\[astro-ph.CO\]/1812.09807](#)].
- [5] A. D. Gow, C. T. Byrnes, P. S. Cole and S. Young, “The power spectrum on small scales: Robust constraints and comparing PBH methodologies,” JCAP **02** (2021), 002 [[\[astro-ph.CO\]/2008.03289](#)].
- [6] Y. Yang, “Constraints on primordial black holes and curvature perturbations from the global 21-cm signal,” Phys. Rev. D **102** (2020) no.8, 083538 [[\[astro-ph.CO\]/2009.11547](#)].
- [7] S. Ando, N. Hiroshima and K. Ishiwata, “Constraining the primordial curvature perturbation using dark matter substructure,” Phys. Rev. D **106** (2022) no.10, 103014 [[\[astro-ph.CO\]/2207.05747](#)].
- [8] S. Matarrese, S. Mollerach and M. Bruni, “Second order perturbations of the Einstein-de Sitter Universe,” Phys. Rev. D **58** (1998), 043504 [[astro-ph/astro-ph/9707278](#)].
- [9] S. Mollerach, D. Harari and S. Matarrese, “CMB polarization from secondary vector and tensor modes,” Phys. Rev. D **69** (2004), 063002 [[astro-ph/astro-ph/0310711](#)].
- [10] Zel’dovich Y.B., 1970, Astron. Astrophys. ,5, 84
- [11] A.G. Doroshkevich, 1970 Astrophysica 6 30
- [12] I. Dalianis and C. Kouvaris, “Gravitational waves from density perturbations in an early matter domination era,” JCAP **07** (2021), 046 [[\[astro-ph.CO\]/2012.09255](#)].
- [13] S. J. Aarseth, “Nbody2: a direct n-body integration code,” New Astron. **6** (2001), 277 [[./astro-ph/0105030](#) [[astro-ph](#)]]
- [14] A. S. Szalay, “Formation of Galaxies,” Nucl. Phys. B **252** (1985), 113-126
- [15] R. Allahverdi, M. A. Amin, A. Berlin, N. Bernal, C. T. Byrnes, M. Sten Delos, A. L. Erickcek, M. Escudero, D. G. Figueroa and K. Freese, *et al.* “The First Three Seconds: a Review of Possible Expansion Histories of the Early Universe,” [[\[astro-ph.CO\]/2006.16182](#)].
- [16] R. Roshan and G. White, “Using gravitational waves to see the first second of the Universe,” [[\[hep-ph\]/2401.04388](#)].
- [17] K. Inomata, K. Kohri, T. Nakama and T. Terada, “Enhancement of Gravitational Waves Induced by Scalar Perturbations due to a Sudden Transition from an Early Matter Era to the Radiation Era,” Phys. Rev. D **100** (2019) no.4, 043532 [[\[astro-ph.CO\]/1904.12879](#)].
- [18] K. Inomata, K. Kohri, T. Nakama and T. Terada, “Gravitational Waves Induced by Scalar Perturbations during a Gradual Transition from an Early Matter Era to the Radiation Era,” JCAP **10** (2019), 071 [[\[astro-ph.CO\]/1904.12878](#)].
- [19] K. N. Ananda, C. Clarkson and D. Wands, “The Cosmological gravitational wave background from primordial density perturbations,” Phys. Rev. D **75** (2007), 123518 [[\[gr-qc\]/gr-qc/0612013](#)].
- [20] D. Baumann, P. J. Steinhardt, K. Takahashi and K. Ichiki, “Gravitational Wave Spectrum Induced by Primordial Scalar Perturbations,” Phys. Rev. D **76** (2007), 084019 [[\[hep-th\]/hep-th/0703290](#)].
- [21] K. A. Malik and D. Wands, “Cosmological perturbations,” Phys. Rept. **475** (2009), 1-51 [[\[astro-ph\]/0809.4944](#)].

- [22] M. Pearce, L. Pearce, G. White and C. Balázs, “Gravitational Wave Signals From Early Matter Domination: Interpolating Between Fast and Slow Transitions,” [[astro-ph.CO/2311.12340](#)].
- [23] T. Papanikolaou, V. Vennin and D. Langlois, JCAP **03** (2021), 053 [[astro-ph.CO/2010.11573](#)].
- [24] G. Domènech, C. Lin and M. Sasaki, “Gravitational wave constraints on the primordial black hole dominated early universe,” JCAP **04** (2021), 062 [erratum: JCAP **11** (2021), E01] [[gr-qc/2012.08151](#)].
- [25] G. Domènech, “Cosmological gravitational waves from isocurvature fluctuations,” AAPPS Bull. **34** (2024) no.1, 4 [[gr-qc/2311.02065](#)].
- [26] K. Inomata, M. Kawasaki, K. Mukaida, T. Terada and T. T. Yanagida, “Gravitational Wave Production right after a Primordial Black Hole Evaporation,” Phys. Rev. D **101** (2020) no.12, 123533 [[astro-ph.CO/2003.10455](#)].
- [27] L. E. Padilla, J. C. Hidalgo and K. A. Malik, “New mechanism for primordial black hole formation during reheating,” Phys. Rev. D **106** (2022) no.2, 023519 [[astro-ph.CO/2110.14584](#)].
- [28] C. M. Yoo, T. Harada, S. Hirano, H. Okawa and M. Sasaki, “Primordial black hole formation from massless scalar isocurvature,” Phys. Rev. D **105** (2022) no.10, 103538 [[gr-qc/2112.12335](#)].
- [29] R. Durrer and A. Kusenko, “Magnetogenesis from early structure formation due to Yukawa forces,” JCAP **11** (2023), 002 [[astro-ph.CO/2209.13313](#)].
- [30] M. M. Flores, A. Kusenko and M. Sasaki, “Gravitational Waves from Rapid Structure Formation on Microscopic Scales before Matter-Radiation Equality,” Phys. Rev. Lett. **131** (2023) no.1, 1 [[astro-ph.CO/2209.04970](#)].
- [31] V. De Luca, G. Franciolini and A. Riotto, “Heavy Primordial Black Holes from Strongly Clustered Light Black Holes,” Phys. Rev. Lett. **130** (2023) no.17, 171401 [[astro-ph.CO/2210.14171](#)].
- [32] G. Domènech, D. Inman, A. Kusenko and M. Sasaki, “Halo formation from Yukawa forces in the very early Universe,” Phys. Rev. D **108** (2023) no.10, 103543 [[astro-ph.CO/2304.13053](#)].
- [33] M. M. Flores, A. Kusenko, L. Pearce, Y. F. Perez-Gonzalez and G. White, “Testing high scale supersymmetry via second order gravitational waves,” Phys. Rev. D **108** (2023) no.12, 123002 [[hep-ph/2308.15522](#)].
- [34] H. Assadullahi and D. Wands, “Gravitational waves from an early matter era,” Phys. Rev. D **79** (2009), 083511 [[astro-ph.CO/0901.0989](#)].
- [35] K. Jedamzik, M. Lemoine and J. Martin, “Generation of gravitational waves during early structure formation between cosmic inflation and reheating,” JCAP **04** (2010), 021 [[astro-ph.CO/1002.3278](#)].
- [36] T. Nakama, “Stochastic gravitational waves associated with primordial black holes formed during an early matter era,” Phys. Rev. D **101** (2020) no.6, 063519
- [37] B. Eggemeier, J. C. Niemeyer, K. Jedamzik and R. Easther, “Stochastic gravitational waves from postinflationary structure formation,” Phys. Rev. D **107** (2023) no.4, 043503 [[astro-ph.CO/2212.00425](#)].
- [38] N. Fernandez, J. W. Foster, B. Lillard and J. Shelton, “Stochastic Gravitational Waves from Early Structure Formation,” [[astro-ph.CO/2312.12499](#)].
- [39] I. Dalianis, “Features in the Inflaton Potential and the Spectrum of Cosmological Perturbations,” [[astro-ph.CO/2310.11581](#)].
- [40] S. Balaji, G. Domènech and G. Franciolini, “Scalar-induced gravitational wave interpretation of PTA data: the role of scalar fluctuation propagation speed,” JCAP **10** (2023), 041 [[gr-qc/2307.08552](#)].

- [41] Z. C. Zhao, Q. H. Zhu, S. Wang and X. Zhang, “Exploring the Equation of State of the Early Universe: Insights from BBN, CMB, and PTA Observations,” [[astro-ph.CO/2307.13574](#)].
- [42] Z. Chang, Y. T. Kuang, D. Wu, J. Z. Zhou and Q. H. Zhu, “New constraints on primordial non-Gaussianity from missing two-loop contributions of scalar induced gravitational waves,” *Phys. Rev. D* **109** (2024) no.4, L041303 [[astro-ph.CO/2311.05102](#)].
- [43] G. Domènech, S. Pi, A. Wang and J. Wang, “Induced Gravitational Wave interpretation of PTA data: a complete study for general equation of state,” [[astro-ph.CO/2402.18965](#)].
- [44] M. Y. Khlopov and A. G. Polnarev, “PRIMORDIAL BLACK HOLES AS A COSMOLOGICAL TEST OF GRAND UNIFICATION,” *Phys. Lett. B* **97** (1980), 383-387
- [45] A. G. Polnarev and M. Y. Khlopov, “COSMOLOGY, PRIMORDIAL BLACK HOLES, AND SUPERMASSIVE PARTICLES,” *Sov. Phys. Usp.* **28** (1985), 213-232
- [46] T. Harada, C. M. Yoo, K. Kohri, K. i. Nakao and S. Jhingan, “Primordial black hole formation in the matter-dominated phase of the Universe,” *Astrophys. J.* **833** (2016) no.1, 61 [[astro-ph.CO/1609.01588](#)].
- [47] T. Harada, C. M. Yoo, K. Kohri and K. I. Nakao, “Spins of primordial black holes formed in the matter-dominated phase of the Universe,” *Phys. Rev. D* **96** (2017) no.8, 083517 [erratum: *Phys. Rev. D* **99** (2019) no.6, 069904] [[gr-qc/1707.03595](#)].
- [48] I. Dalianis, A. Kehagias and G. Tringas, “Primordial black holes from α -attractors,” *JCAP* **01** (2019), 037 [[astro-ph.CO/1805.09483](#)].
- [49] T. Kokubu, K. Kyutoku, K. Kohri and T. Harada, “Effect of Inhomogeneity on Primordial Black Hole Formation in the Matter Dominated Era,” *Phys. Rev. D* **98** (2018) no.12, 123024 [[astro-ph.CO/1810.03490](#)].
- [50] G. Ballesteros, J. Rey and F. Rompineve, “Detuning primordial black hole dark matter with early matter domination and axion monodromy,” *JCAP* **06** (2020), 014 [[astro-ph.CO/1912.01638](#)].
- [51] V. De Luca, G. Franciolini, A. Kehagias, P. Pani and A. Riotto, “Primordial black holes in matter-dominated eras: The role of accretion,” *Phys. Lett. B* **832** (2022), 137265 [[astro-ph.CO/2112.02534](#)].
- [52] J. Garcia-Bellido, M. Peloso and C. Unal, “Gravitational Wave signatures of inflationary models from Primordial Black Hole Dark Matter,” *JCAP* **09** (2017), 013 [[astro-ph.CO/1707.02441](#)].
- [53] I. Dalianis and K. Kritos, “Exploring the Spectral Shape of Gravitational Waves Induced by Primordial Scalar Perturbations and Connection with the Primordial Black Hole Scenarios,” *Phys. Rev. D* **103** (2021) no.2, 023505 [[astro-ph.CO/2007.07915](#)].
- [54] J. Fumagalli, S. é. Renaux-Petel and L. T. Witkowski, “Resonant features in the stochastic gravitational wave background,” *JCAP* **08** (2021), 059 [[astro-ph.CO/2105.06481](#)].
- [55] I. Dalianis, G. P. Kodaxis, I. D. Stamou, N. Tetradis and A. Tsigkas-Kouvelis, “Spectrum oscillations from features in the potential of single-field inflation,” *Phys. Rev. D* **104** (2021) no.10, 103510 [[astro-ph.CO/2106.02467](#)].
- [56] C. Yuan and Q. G. Huang, “A topic review on probing primordial black hole dark matter with scalar induced gravitational waves,” *iScience* **24** (2021), 102860 [[astro-ph.GA/2103.04739](#)].
- [57] G. Domènech, “Scalar Induced Gravitational Waves Review,” *Universe* **7** (2021) no.11, 398 [[gr-qc/2109.01398](#)].
- [58] C. Chen, A. Ota, H. Y. Zhu and Y. Zhu, “Missing one-loop contributions in secondary gravitational waves,” *Phys. Rev. D* **107** (2023) no.8, 083518 [[astro-ph.CO/2210.17176](#)].
- [59] S. Balaji, G. Domenech and J. Silk, “Induced gravitational waves from slow-roll inflation after an enhancing phase,” *JCAP* **09** (2022), 016 [[astro-ph.CO/2205.01696](#)].

- [60] D. S. Meng, C. Yuan and Q. G. Huang, “Primordial black holes generated by the non-minimal spectator field,” *Sci. China Phys. Mech. Astron.* **66** (2023) no.8, 280411 [[astro-ph.CO/2212.03577](#)].
- [61] K. Boutivas, I. Dalianis, G. P. Kodaxis and N. Tetradis, “The effect of multiple features on the power spectrum in two-field inflation,” *JCAP* **08** (2022) no.08, 021 [[astro-ph.CO/2203.15605](#)].
- [62] S. Choudhury, K. Dey, A. Karde, S. Panda and M. Sami, “Primordial non-Gaussianity as a saviour for PBH overproduction in SIGWs generated by Pulsar Timing Arrays for Galileon inflation,” [[astro-ph.CO/2310.11034](#)].
- [63] G. Franciolini, A. Iovino, Junior., V. Vaskonen and H. Veermae, “Recent Gravitational Wave Observation by Pulsar Timing Arrays and Primordial Black Holes: The Importance of Non-Gaussianities,” *Phys. Rev. Lett.* **131** (2023) no.20, 201401 [[astro-ph.CO/2306.17149](#)].
- [64] C. Yuan, D. S. Meng and Q. G. Huang, “Full analysis of the scalar-induced gravitational waves for the curvature perturbation with local-type non-Gaussianities,” *JCAP* **12** (2023), 036 [[astro-ph.CO/2308.07155](#)].
- [65] A. Iannicari, A. J. Iovino, A. Kehagias, D. Perrone and A. Riotto, “The Primordial Black Hole Abundance: The Broader, the Better,” [[astro-ph.CO/2402.11033](#)].
- [66] G. Domènech and M. Sasaki, “Probing Primordial Black Hole Scenarios with Terrestrial Gravitational Wave Detectors,” [[gr-qc/2401.07615](#)].
- [67] V. Mukhanov, Cambridge University Press, 2005, ISBN 978-0-521-56398-7
- [68] D. Lynden-Bell, “Statistical mechanics of violent relaxation in stellar systems,” *Mon. Not. Roy. Astron. Soc.* **136** (1967), 101-121
- [69] B. S. Sathyaprakash and B. F. Schutz, “Physics, Astrophysics and Cosmology with Gravitational Waves,” *Living Rev. Rel.* **12** (2009), 2 [[gr-qc/0903.0338](#)].
- [70] M. Maggiore, “Gravitational wave experiments and early Universe cosmology,” *Phys. Rept.* **331** (2000), 283-367 [[gr-qc/gr-qc/9909001](#)].
- [71] C. Caprini and D. G. Figueroa, “Cosmological Backgrounds of Gravitational Waves,” *Class. Quant. Grav.* **35** (2018) no.16, 163001 [[astro-ph.CO/1801.04268](#)].
- [72] G. M. Harry [LIGO Scientific], “Advanced LIGO: The next generation of gravitational wave detectors,” *Class. Quant. Grav.* **27** (2010), 084006
- [73] F. Acernese [Virgo], “The Advanced Virgo detector,” *J. Phys. Conf. Ser.* **610** (2015) no.1, 012014 doi:10.1088/1742-6596/610/1/012014
- [74] T. Akutsu *et al.* [KAGRA], “Overview of KAGRA: Detector design and construction history,” *PTEP* **2021** (2021) no.5, 05A101 [[physics.ins-det/2005.05574](#)].
- [75] B. Sathyaprakash, M. Abernathy, F. Acernese, P. Ajith, B. Allen, P. Amaro-Seoane, N. Andersson, S. Aoudia, K. Arun and P. Astone, *et al.* “Scientific Objectives of Einstein Telescope,” *Class. Quant. Grav.* **29** (2012), 124013 [erratum: *Class. Quant. Grav.* **30** (2013), 079501] [[gr-qc/1206.0331](#)].
- [76] P. Amaro-Seoane *et al.* [LISA], “Laser Interferometer Space Antenna,” [[astro-ph.IM/1702.00786](#)].
- [77] W. H. Ruan, Z. K. Guo, R. G. Cai and Y. Z. Zhang, “Taiji program: Gravitational-wave sources,” *Int. J. Mod. Phys. A* **35** (2020) no.17, 2050075 [[gr-qc/1807.09495](#)].
- [78] J. Luo *et al.* [TianQin], “TianQin: a space-borne gravitational wave detector,” *Class. Quant. Grav.* **33** (2016) no.3, 035010 [[astro-ph.IM/1512.02076](#)].
- [79] N. Seto, S. Kawamura and T. Nakamura, “Possibility of direct measurement of the acceleration of the Universe using 0.1-Hz band laser interferometer gravitational wave antenna in space,” *Phys. Rev. Lett.* **87** (2001), 221103 [[astro-ph/astro-ph/0108011](#)].
- [80] S. Sato, S. Kawamura, M. Ando, T. Nakamura, K. Tsubono, A. Araya, I. Funaki, K. Ioka, N. Kanda and S. Moriwaki, *et al.* “The status of DECIGO,” *J. Phys. Conf. Ser.* **840** (2017) no.1, 012010

- [81] J. Crowder and N. J. Cornish, “Beyond LISA: Exploring future gravitational wave missions,” *Phys. Rev. D* **72** (2005), 083005 [[\[gr-qc\]/gr-qc/0506015](#)].
- [82] A. Sesana, N. Korsakova, M. A. Sedda, V. Baibhav, E. Barausse, S. Barke, E. Berti, M. Bonetti, P. R. Capelo and C. Caprini, *et al.* “Unveiling the gravitational universe at μ -Hz frequencies,” *Exper. Astron.* **51** (2021) no.3, 1333-1383 [[\[astro-ph.IM\]/1908.11391](#)].
- [83] G. Agazie *et al.* [NANOGrav], “The NANOGrav 15 yr Data Set: Evidence for a Gravitational-wave Background,” *Astrophys. J. Lett.* **951** (2023) no.1, L8 [[\[astro-ph.HE\]/2306.16213](#)].
- [84] G. Agazie *et al.* [NANOGrav], “The NANOGrav 15 yr Data Set: Observations and Timing of 68 Millisecond Pulsars,” *Astrophys. J. Lett.* **951** (2023) no.1, L9 [[\[astro-ph.HE\]/2306.16217](#)].
- [85] A. Afzal *et al.* [NANOGrav], “The NANOGrav 15 yr Data Set: Search for Signals from New Physics,” *Astrophys. J. Lett.* **951** (2023) no.1, L11 [[\[astro-ph.HE\]/2306.16219](#)].
- [86] J. Antoniadis *et al.* [EPTA], “The second data release from the European Pulsar Timing Array III. Search for gravitational wave signals,” *Astron. Astrophys.* **678** (2023), A50 [[\[astro-ph.HE\]/2306.16214](#)].
- [87] J. Antoniadis *et al.* [EPTA], “The second data release from the European Pulsar Timing Array I. The dataset and timing analysis,” *Astron. Astrophys.* **678** (2023), A48 [[\[astro-ph.HE\]/2306.16224](#)].
- [88] J. Antoniadis *et al.* [EPTA], “The second data release from the European Pulsar Timing Array: V. Implications for massive black holes, dark matter and the early Universe,” [[\[astro-ph.CO\]/2306.16227](#)].
- [89] G. Agazie *et al.* [International Pulsar Timing Array], “Comparing recent PTA results on the nanohertz stochastic gravitational wave background,” [[\[astro-ph.HE\]/2309.00693](#)].
- [90] D. J. Reardon, A. Zic, R. M. Shannon, G. B. Hobbs, M. Bailes, V. Di Marco, A. Kapur, A. F. Rogers, E. Thrane and J. Askew, *et al.* “Search for an Isotropic Gravitational-wave Background with the Parkes Pulsar Timing Array,” *Astrophys. J. Lett.* **951** (2023) no.1, L6 [[\[astro-ph.HE\]/2306.16215](#)].
- [91] A. Zic, D. J. Reardon, A. Kapur, G. Hobbs, R. Mandow, M. Curyło, R. M. Shannon, J. Askew, M. Bailes and N. D. R. Bhat, *et al.* “The Parkes Pulsar Timing Array Third Data Release,” [[\[astro-ph.HE\]/2306.16230](#)].
- [92] D. J. Reardon, A. Zic, R. M. Shannon, V. Di Marco, G. B. Hobbs, A. Kapur, M. E. Lower, R. Mandow, H. Middleton and M. T. Miles, *et al.* “The Gravitational-wave Background Null Hypothesis: Characterizing Noise in Millisecond Pulsar Arrival Times with the Parkes Pulsar Timing Array,” *Astrophys. J. Lett.* **951** (2023) no.1, L7 [[\[astro-ph.HE\]/2306.16229](#)].
- [93] H. Xu, S. Chen, Y. Guo, J. Jiang, B. Wang, J. Xu, Z. Xue, R. N. Caballero, J. Yuan and Y. Xu, *et al.* “Searching for the Nano-Hertz Stochastic Gravitational Wave Background with the Chinese Pulsar Timing Array Data Release I,” *Res. Astron. Astrophys.* **23** (2023) no.7, 075024 [[\[astro-ph.HE\]/2306.16216](#)].
- [94] G. Janssen, G. Hobbs, M. McLaughlin, C. Bassa, A. T. Deller, M. Kramer, K. Lee, C. Mingarelli, P. Rosado and S. Sanidas, *et al.* “Gravitational wave astronomy with the SKA,” *PoS AASKA14* (2015), 037 [[\[astro-ph.IM\]/1501.00127](#)].
- [95] J. D. Barrow, E. J. Copeland and A. R. Liddle, “The Cosmology of black hole relics,” *Phys. Rev. D* **46** (1992), 645-657
- [96] J. C. Hidalgo, L. A. Urena-Lopez and A. R. Liddle, “Unification models with reheating via Primordial Black Holes,” *Phys. Rev. D* **85** (2012), 044055 [[\[astro-ph.CO\]/1107.5669](#)].
- [97] I. Dalianis and G. Tringas, “Primordial black hole remnants as dark matter produced in thermal, matter, and runaway-quintessence postinflationary scenarios,” *Phys. Rev. D* **100** (2019) no.8, 083512 [[\[astro-ph.CO\]/1905.01741](#)].

- [98] I. Dalianis and G. P. Kodaxis, “Reheating in Runaway Inflation Models via the Evaporation of Mini Primordial Black Holes,” *Galaxies* **10** (2022) no.1, 31 [[\[astro-ph.CO\]/2112.15576](#)].
- [99] G. Domènech and M. Sasaki, “Gravitational wave hints black hole remnants as dark matter,” *Class. Quant. Grav.* **40** (2023) no.17, 177001 [[\[gr-qc\]/2303.07661](#)].
- [100] G. Franciolini and P. Pani, “Stochastic gravitational-wave background at 3G detectors as a smoking gun for microscopic dark matter relics,” *Phys. Rev. D* **108** (2023) no.8, 083527 [[\[astro-ph.CO\]/2304.13576](#)].